Conductivity of UO2 ceramics: effect of a weakly to strongly branched pore network up to 500°C (exp) and numerical simulations beyond

Léo Moutin, Joane Meynard, Marc Josien, Michel Bornert, Christelle Duguay, Frederic Adenot, Laurent Fayette, Renaud Masson

Conductivity of UO_2 ceramics: effect of a weakly to strongly branched pore network up to 500 °C (exp) and numerical simulations beyond

Léo Moutin[a], Marc Josien[a], Michel Bornert[b], Christelle Duguay[a], Frédéric Adenot[a], Laurent Fayette[a], Renaud Masson[a,*]

[a] *CEA, DES, IRESNE, DEC, Cadarache F-13018 Saint-Paul-lez-Durance, France*
[b] *Laboratoire Navier, Ecole des ponts, Univ. Gustave Eiffel, CNRS, 6-8 avenue Blaise Pascal, Champs-sur-Marne, 77455 Marne-la-Vallée Cedex*

Abstract

We consider in this study three uranium dioxide ceramics whose porous network varies noticeably according to the manufacturing conditions. This porous network is characterized by a fine and elongated porosity which is made up of inter-granules pores but also of occluded pores which can be spotted at a much smaller scale. Thermal diffusivity measurements have been performed by a flash method on these ceramics at 50 °C under different atmospheres but also up to 500 °C under an argon and dihydrogen atmosphere. These measurements have shown marked differences in the thermal conductivities of the three ceramics, in particular a sharp degradation when the open porosity increases is reported. To understand the influence of these two families of porosities on the effective conductivity, a two-scale model has been developed. The effect of the occluded porosity is approximated using the Maxwell (1873) model. The effect of the inter-granules porosity is evaluated by full-field numerical simulations performed on synthetic microstructures generated by the optimization process described in Moutin et al. (2023). Comparisons of model predictions to experimental results confirm the predominant role of the inter-granules porosity on the effective conductivity. Besides, it is shown that the Knudsen effect must be taken into account to accurately predict the variations in thermal conductivity of ceramics depending on the gas contained in the inter-granules pores at 50 °C. Finally, the simulated conductivities of the ceramics are shown to predict temperatures effects up to 500 °C.

Keywords: UO_2 Ceramics, Thermal Conductivity, Inter-granules Pores, Homogenization, Virtual microstructures, FFT Computation

1. Introduction

Knowledge of the physical behavior of the materials that make up industrial structures is essential for predicting the phenomena that will occur during their service life. This is particularly the case for ceramics used as fuel in nuclear power plants. The evolution of their

*Corresponding author
Email address: renaud.masson@cea.fr (Renaud Masson)

thermal conductivity, which may degrade under the effects of temperature and irradiation, is a very sensitive point. Among the factors which may drive their thermal conductivity in the virgin state as well as their potential degradation under irradiation, porosity plays a dominant role. This is why the porous network affecting the microstructure of nuclear fuels is especially examined.

The physical behavior of materials is highly dependent on the characteristics of their microstructure and, in the case of porous solids, in particular on the morphology of their pores (see for instance Torquato and Haslach Jr (2002)). Numerous studies have been carried out to determine the influence of porosity on the thermal conductivity of UO_2 ceramics (see among other Ondracek and Schulz (1973); Brandt and Neuer (1976); Harding and Martin (1989)). In general, the porosity remains small (less than a few percent) and has thus moderate effects on the thermal conductivity at least for standard UO_2 ceramics. Hence, the models take generally the form of a correction depending on the porosity. This correction factor, recommended in particular by IAEA (2006), was introduced by Brandt and Neuer (1976) and predicts a linear decrease in conductivity with temperature. The variations of the only parameter appearing in this correction seem to be mainly induced by the manufacturing process of UO_2 ceramics, as suggested by MacEwan et al. (1967).

The materials under consideration here are porous UO_2 ceramics, obtained by sintering powder compacts made of multicrystalline granules. Yet, they differ from standard UO_2 ceramics since the standard fabrication process has been modified to obtain ceramics with a more or less extended porous network. Indeed, these non standard ceramics have been extensively characterized in 2D by optical microscopy with the development of specific morphological descriptors to quantify the porous network and its possible anisotropy. This study, which is described in detail in Moutin et al. (2023), has shown that some of these microstructures display an extremely developed porous network. The ceramics under consideration have also been imaged in 3D by synchrotron X-Ray micro-computed tomography, images confirming the 3D interconnection of the porous network (see Moutin et al. (2024)).

Among potential nuclear fuels for Generation IV fast reactors, mixed uranium-plutonium carbides fuels operate at low temperature. As explained in Duguay and Pelloquin (2015), a large interconnected porous network may be of great interest by favoring the release of fission gases during irradiation of nuclear fuels. But these interconnected pores act as thermal barriers and therefore may have detrimental effects on the conductivity of the ceramics. In this respect, the non-standard UO_2 ceramics described above are of great interest and should be seen as model ceramics with a more or less developed open porosity network. To quantify this potential detrimental effect, 3D virtual microstructures of these UO_2 ceramics have been developped. These virtual microstructures derive from a morphological model depending on a limited number of parameters (see Meynard et al. (2022)). In the reference Moutin et al. (2023) cited above, these parameters have been tuned in order to mimic optical images of the real ceramics. Next, 2D numerical simulations have been performed on processed images of reference ceramics and on cross-sections extracted from the tuned 3D morphological model. The good agreement provides some confidence on the pertinence of the tuned 3D morphological model and suggests that the porous network has a strong effect on the thermal conductivity of these ceramics.

Hence why the objective of this work is firstly to measure the effective conductivity of the ceramics characterized in Moutin et al. (2023) to quantify experimentally the effect of the

porous network. In addition, and in order to interpret these measurements and extrapolate them to other conditions (temperatures higher than those considered here, alternative gaseous environment, irradiation, etc.), we also propose to simulate the effective conductivity of these ceramics. For these 3D simulations, we will use the morphological model proposed by Meynard et al. (2022) and tuned by Moutin et al. (2023) on the ceramics under consideration.

The paper is organized as follows. The first two sections are dedicated to the experimental investigation of the thermal behavior of the UO_2 ceramics under consideration. Before presenting the results in Section 3, we briefly review in Section 2 the main microstructural characteristics of these ceramics and the protocol used for thermal diffusivity measurement. To interpret these measurements and understand the main phenomena controlling the thermal behavior of these ceramics, a two-scale model for effective conductivities was developed. On the largest scale, we make use of a 3D full-field simulation on a Representative Volume Element, capitalizing on a previously developed 3D model for microstructures of the ceramics of interest. This model is presented in Section 4. Comparisons between the experiments and the predictions of this model are reported in the final Section 5.

2. Material and measurement device

2.1. Material

As explained in the introduction, the ceramics under consideration have been manufactured by an alternative process to the one traditionally used (known as the standard process, see Moutin et al. (2023)). Optical microscopy images of ceramics obtained from the standard and the alternative processes are reported in Figure 1-left and Figure 1-right respectively. Like the ceramics manufactured using the standard process, the ceramics under consideration feature a distribution of micrometric-sized intra-granules pores that appear quasi-spherical. However, unlike the ceramics produced by the standard process, these ceramics also show a network of large and slender pores. Thus, two families of pores are observed in the ceramics obtained by the alternative process:

- Small and quasi-spherical pores that are called "occluded" pores and assimilated to closed porosity. The effect of these pores on the thermal behavior of ceramics is thought to be relatively small.

- Pores with a slender shape and a larger size, located at the joints between the granules and therefore called "inter-granules"[1] pores. Due to the slender shape of the pores, interconnections are visible on the surface and are expected in the volume, which could lead to the overall interconnection of these pores, forming a true network. This is why the volume of these pores is identified with that of the open porosity. As these pores act as thermal barriers, their effect on the thermal behavior of ceramics is expected to be of first order.

In order to study the relationship between the porosity present in fuels and their thermal properties, various model ceramics have been manufactured. The manufacturing conditions

[1] "Inter-granular" is also a currently used expression.

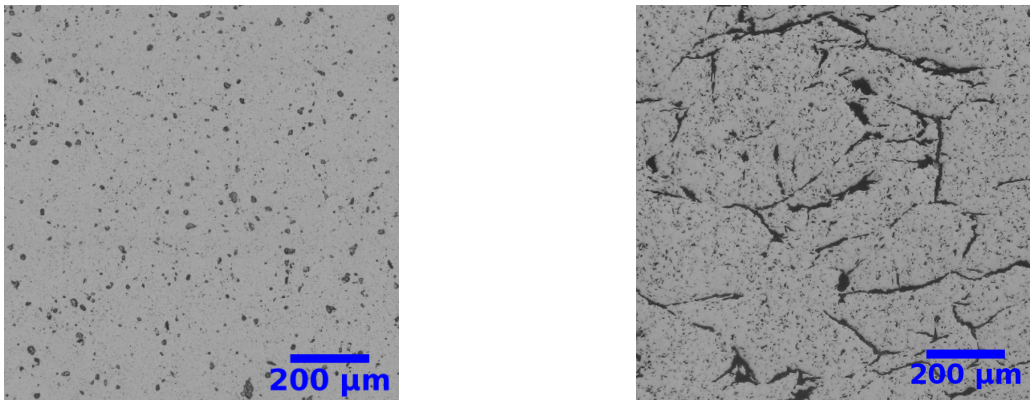

Figure 1: Optical microscopy images of ceramics obtained from the standard process (left) and the alternative process (right).

for these ceramics were chosen and optimized to obtain samples with different characteristics, particularly in terms of the volume fraction of closed porosity (associated with the occluded porosity) and open porosity (associated with the inter-granules porosity). Three model ceramics, C_1, C_3 and C_{3^*}, which have already been the subject of work reported in Moutin et al. (2023), are studied here. The open (c_o), closed (c_{cl}) and total (c_T) porosity volume fractions of these ceramics are given in Table 1. The volume fraction of total porosity can be calculated by measuring the bulk density of the porous solid and comparing it with the theoretical density of the 100 % dense solid. The volume fraction of open porosity can be obtained by various experimental techniques, in particular by immersion in a wetting liquid (Pinot, 2015). As this porosity is assumed to be fully accessible to the liquid, its volume fraction can be obtained by comparing the bulk density of the solid with that determined after immersion. Finally, the volume fraction of the closed porosity can be determined by subtracting the volume fraction of the total porosity from the volume fraction of the open porosity. The uncertainty related to the measurement of c_T, c_o and c_{cl} is about $\pm 0.2\%$.

Ceramics	C_1	C_3	C_{3^*}
c_o (%)	0.9	3.45	3.45
c_{cl} (%)	2.0	1.6	1.0
c_T (%)	2.9	5.05	4.45

Table 1: List of model ceramics on which diffusivity measurements have been carried out and their characteristics, i.e. open (c_o), closed (c_{cl}) and total (c_T) porosity volume fractions. Uncertainties equal $\pm 0.2\%$ for each characteristic c_T, c_o and c_{cl}.

2.2. Characterization of microstructures C_1, C_3 and C_{3*}

In order to extract the main characteristics of the porous network of these ceramics in relation to their thermal properties, they were extensively characterized.

Indeed, based on $2D$ optical microscopy (see Figures 2), a thorough characterization of the porous network of these ceramics was carried out. As explained in more details in Moutin

et al. (2023), an image processing protocol has been set up to convert optical microscopy images into skeletonized binary images from which it is possible to extract informations about the porous network (elongation, orientation and spatial distribution of the pore network). As these skeletonized images have shown clear differences between these microstructures, particular morphological descriptors have been used to quantify these differences. This analysis have evidenced that :

- The porous network is much more extended and branched for C_3 and C_{3*} than C_1. On the other hand, C_3 and C_{3*} have an equally well-developed network, which is consistent with the fact that they have the same open porosity ;
- In contrast to C_1 and C_3, the porous network of ceramic C_{3*} is more elongated in one direction which corresponds to the horizontal direction in Figure 2. This was quantified thanks to a morphological indicator called the length of the intercepts (see Figure 5 in Moutin et al. (2023)) ;
- 2D full-field numerical simulations (based on the FFT method presented in Section 4.3) have been performed on processed images of reference ceramics and suggest that the conductivity of the three ceramics depends strongly on their porous networks.

As mentioned above, the two pore families identified in the studied UO_2 ceramics are present at quite different scales. This scale separation is clearly visible when observing the microstructures of the ceramics of interest using optical microscopy (see images in Figure 2). So, and we will come back to this point later in Section 4, we rely on this principle of scale separation to study separately the relative effects of these two pore families on the thermal properties of ceramics.

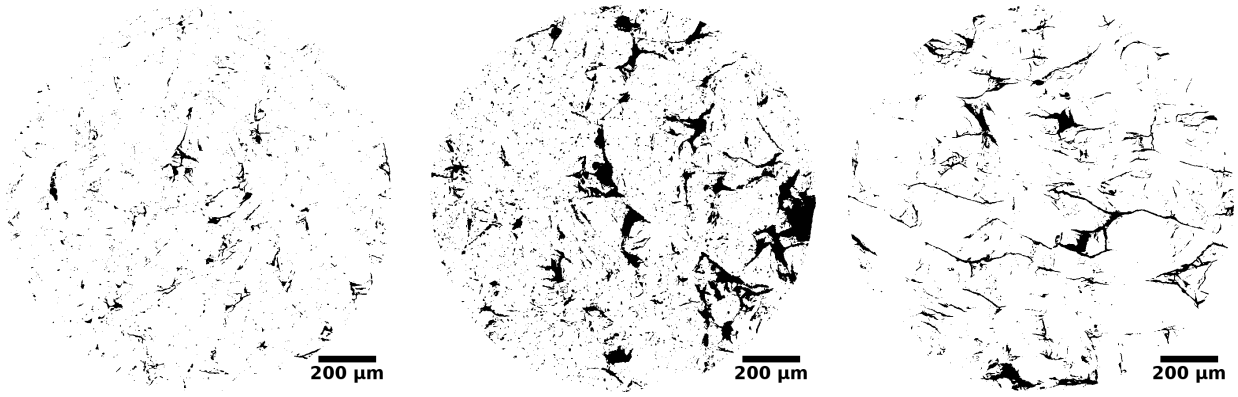

Figure 2: Regions of interest extracted from optical microscopy images of the three studied ceramics showing the size separation between intra and inter-granules pores. From left to right: C_1, C_3 and C_{3^*}.

Finally, and as illustrated in Figure 3, ceramics C_1 and C_3 have also been imaged in 3D by X-Ray micro-computed tomography on the Psiché beamline of the Soleil synchrotron (https://www.synchrotron-soleil.fr). As reported in (Moutin et al., 2024; Moutin, 2023), a specific setup adapted to the very strong attenuation of UO_2 was needed to obtain these 3D images. On Figure 3, the extent of the obtained pore network visually appears to be consistent with their open porosity. We will come back to the insights provided by these 3D images below, especially in Sections 3.1 and 4.

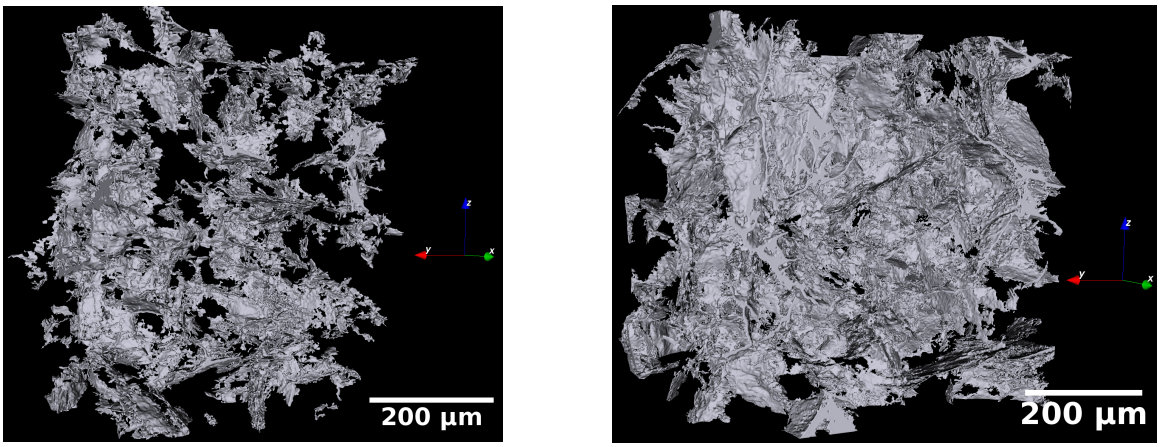

Figure 3: 3D views of the porous network of C_1 (on the left) and C_3 (on the right) ceramics obtained from tomographic images.

2.3. Measurement device

Thermal conductivity λ ($\mathrm{W.m^{-1}.K^{-1}}$) , which gives the ability of a material to conduct heat flow, is defined by Fourier's Law (Fourier, 1822). Under the assumption of linearity and isotropy, it relates the the heat flux density vector Φ ($\mathrm{W.m^{-2}}$) with the temperature gradient ∇T ($\mathrm{K.m^{-1}}$) as follows:

$$\Phi = -\lambda \nabla T \tag{1}$$

To characterize the thermal behavior of UO_2, flash method is becoming increasingly popular (Parker et al., 1961; Hay et al., 2017; Fall, 1995). It has the advantage of being non-destructive, applicable to a wide range of materials and compatible with high temperature measurements. The principle of the flash method is to apply a pulse of light to the front face of the sample to excite it thermally and then to measure the temperature change in response to this pulse on the rear face of the sample. This method makes it possible to measure the thermal diffusivity $\mathcal{D}$ of materials, which is related to their conductivity by the relation (2):

$$\lambda = \rho \, C_p \, \mathcal{D} \tag{2}$$

where ρ ($kg.m^{-3}$) is the bulk density and $C_p(J.kg^{-1}.K^{-1})$ is the specific heat capacity of the dense solid.

Still in the context of an application to UO_2, authors have been interested in extending the range of diffusivity measurements by the flash method to reach temperatures up to the melting point in order to study its behavior under accidental conditions (Vlahovic et al., 2018). Studies are also underway to develop a method for measuring the thermal diffusivity of irradiated ceramics in hot cells (Doualle et al., 2021). This new approach will be of great interest to the work presented in this paper, as it is planned to study the effects of irradiation on the thermal behavior of the ceramics of interest in the near future.

In order to study their thermal behavior, thermal diffusivity measurements using the flash method were carried out on the ceramics of interest using the HyperFlash LFA 467 instrument (Netzsch). The source that generates the pulse on the front side is a xenon lamp that emits a flash with a diameter of 25 mm, and the measurement on the rear side is carried out with an indium antimonide-based infrared detector that records the temporal evolution

of the signal over an area in the centre of the sample. The spot size, i.e. the area over which the time response is recorded, is set at 5 mm. To improve the signal response, a thin layer of graphite is deposited on the samples prior to measurement. This graphite layer concentrates the energy and limits its reflection from the sample. It has also been shown to have no effect on the thermal behavior of the samples (Maillet et al., 2000). The experimental uncertainty associated with these flash measurements is around 3 %[2]. The thermal diffusivity of ceramics was measured along the pressing direction during the compaction step of the fabrication process.

Figure 4 shows an experimental thermogram recorded on the rear side of one of our samples tested at 200 °C. The thermal curve gives the rise in temperature (signal in Volts) as a function of time. Similar thermal curves were obtained for the ceramics tested up to 500 °C. The decrease after obtaining the maximum value of temperature is due to the non-adiabatic nature of the experiment. As heat losses increase, the temperature of the rear surface of the sample drops after it reaches a peak. The absence of a high temperature increase in the detector signal immediately after the shot (which corresponds to the time 0 ms) makes it possible to neglect the contribution of radiation to heat transfer in the temperature range studied.

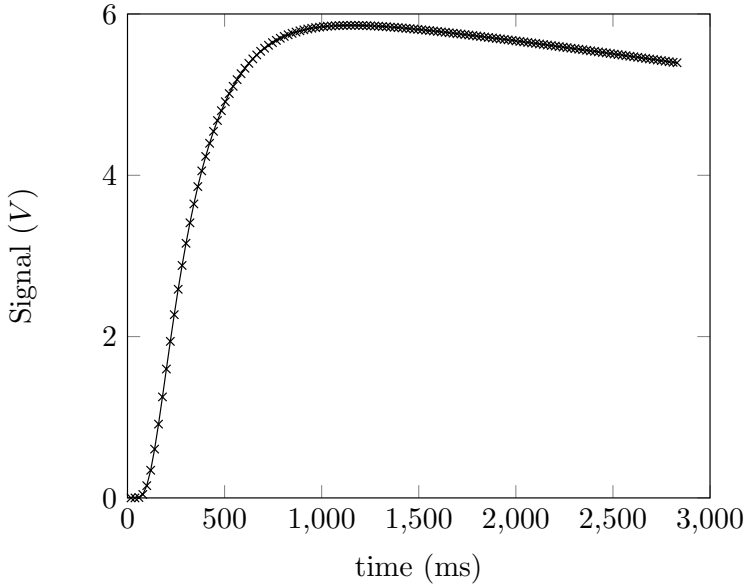

Figure 4: Thermogram recorded at 200 °C (ceramic C_{3^*}).

2.4. Determination of the thermal conductivity from a thermal diffusivity measurement

Experimental measurements provide access to the thermal diffusivity of the ceramics of interest. As explained above (see Relation (2)), the thermal conductivity can be deduced from

[2]The thermal diffusivity of standard samples (Pyroceram®) with different geometries was measured and compared to that obtained by the French National Metrology and Testing Laboratory (LNE) for one of the samples. The values obtained were very close and 2 to 3.2 % higher than the value measured at the LNE, i.e. in the upper range of the uncertainty range given by the LNE (± 3 %).

the diffusivity provided that the apparent density ρ as well as the specific heat capacity C_p are known at the considered temperature. The apparent density takes into account the changes in volume caused by the thermal expansion of the ceramic. Its evolution with temperature is given by the equation (3)[3].

$$\rho(T) = \frac{\rho_0}{(1 + \alpha(T).(T - T_0))^3} \tag{3}$$

In this expression, ρ_0 is the bulk density at room temperature ($T_0 = 273\,K$) and α is the coefficient of linear thermal expansion in K^{-1}, whose expression was introduced by Martin (1988) and is recommended by Carbajo et al. (2001), namely:

$$\alpha(T) = \begin{cases} 9.828 \times 10^{-6} - 6.39 \times 10^{-10}T + 1.33 \times 10^{-12}T^2 - 1.757 \times 10^{-17}T^3 \\ \text{for } 273\text{K} \leq T \leq 923\text{K} \\ \\ 1.1833 \times 10^{-5} - 5.013 \times 10^{-9}T + 3.756 \times 10^{-12}T^2 - 6.125 \times 10^{-17}T^3 \\ \text{for } 923\text{K} \leq T \leq 3120\text{K} \end{cases} \tag{4}$$

The specific heat capacity of the dense ceramic is determined using the correlation given by the equation (5) introduced by Fink (2000), and recommended by Carbajo et al. (2001), where $t = T(K)/1000$:

$$C_p(T) = 52.1743 + 87.951\,t - 84.2411\,t^3 - 2.6334\,t^4 - 0.71391\,t^{-2} \tag{5}$$

Using the relations (2) to (5), the thermal conductivity of the samples can be determined from the experimental diffusivity measurements at a given temperature T.

3. Results

Using the experimental device described above, two measurement campaigns have been carried out:

1. A series of measurements at 50 °C under different atmospheres (air, vacuum and helium) to study the effect of the gaseous environment on the diffusivity of ceramics. These measurements are carried out at 50 °C to ensure that they are independent of temperature variations outside the instrument.

2. A series of measurements up to 500 °C under an argon and dihydrogen atmosphere to avoid oxidation of the sample. The aim is to assess the effect of temperature on the thermal behavior of ceramics.

All measurements are taken in the pressing direction. In the following only the thermal conductivity values are presented.

[3]This relation is derived by considering at T_0 a given volume $V(T_0)$ of the ceramic. For a given temperature $T > T_0$, this ceramic occupies a volume $V(T) > V(T_0)$ as a result of thermal expansion, namely: $V(T)/V(T_0) = (1 + \alpha(T).(T - T_0))^3$. As the mass of the considered ceramic is constant, we obtain:

$$V(T_0)\,\rho_0 = V(T)\,\rho(T) \Rightarrow \rho(T) = \rho_0\,(V(T_0)\,/\,V(T)).$$

3.1. At 50 °C in various gaseous environments

Table 2 gives the values measured for the ceramics C_1, C_3 and C_{3^*} at 50 °C in the three gaseous environments.

C_1			C_3			C_{3^*}		
	$\tilde{\lambda}$	Deviation from measurements in air (%)		$\tilde{\lambda}$	Deviation from measurements in air (%)		$\tilde{\lambda}$	Deviation from measurements in air (%)
Vac	7.60	-0.07	Vac	6.67	-0.5	Vac	5.88	-1.7
Air	7.60	/	Air	6.70	/	Air	5.98	/
He	7.61	0.03	He	6.79	1.4	He	6.16	2.9

Table 2: Thermal conductivities ($W.m^{-1}.K^{-1}$) obtained from experimental measurements of thermal diffusivity using the rear-side flash method on C_1, C_3 and C_{3^*} ceramics at 50 °C in the three gaseous environments. Measurements were taken in the pressing direction. The experimental uncertainty is around 3%.

The three ceramics have significantly different thermal conductivities. This is particularly true for the C_3 and C_{3^*} ceramics, despite having an identical volume fraction of open porosity and virtually the same volume fraction of closed porosity. The main difference between these two ceramics is that the C_{3^*} ceramic has a pore network that is strongly oriented along the axis perpendicular to the pressing one, as identified by Moutin et al. (2023). This orientation of the pore network degrades the thermal conductivity in the pressing direction because the proportion of thermal barriers oriented in the perpendicular direction is greater. This underlines the importance of taking into account the anisotropy of the ceramic C_{3^*}.

Another remarkable point is the low dependence of the measured thermal conductivity on the gaseous environment. This is quite surprising and two main hypotheses have been put forward to explain this behavior. The first is that the porous network is not fully interconnected and therefore not fully accessible to the gas. As a result, part of the network would be filled by the sintering gas when the ceramics are sintered (dihydrogen, which is more conductive than helium). However, a study of the 3D interconnection of the ceramics in question, based on tomographic images obtained at Soleil synchrotron, clearly shows that for highly porous ceramics such as C_3 and C_{3^*}, this network is almost completely interconnected (Moutin, 2023). The first hypothesis therefore seems unlikely. The second hypothesis is that a physical phenomenon could strongly degrade the thermal conductivity of gases, and in particular that of helium: the Knudsen effect. A detailed study of this effect and its consequences for the conductivity of the ceramics is given in Section 5.2.

3.2. Up to 500 °C under an argon with 5 % dihydrogen atmosphere

Table 3 gives the thermal conductivity values obtained for the ceramics of interest between 50 °C and 500 °C under Ar/5 % H_2. It should be noted that measurements at 50 °C were systematically taken upon returning to room temperature to ensure that there was no degradation of the ceramics.

The marked difference in thermal conductivity between the three ceramics, observed at 50 °C in the three gaseous environments, was again observed. Although the thermal conductivity of gases increases with temperature, the conductivity of the ceramics decreases with temperature, as does that of the dense UO_2 (see Appendix A). In addition, the decrease

C_1			C_3			C_{3^*}		
T (°C)	$\tilde{\lambda}$	Deviation from measurements at 50 °C (%)	T (°C)	$\tilde{\lambda}$	Deviation from measurements at 50 °C (%)	T (°C)	$\tilde{\lambda}$	Deviation from measurements at 50 °C (%)
50	7.63	/	50	6.64	/	50	5.98	/
100	7.19	-6	100	6.26	-6	100	5.63	-6
200	6.31	-17	200	5.5	-17	200	4.99	-17
300	5.58	-27	300	4.89	-26	300	4.45	-26
400	4.97	-35	400	4.36	-34	400	4.00	-33
500	4.52	-41	500	3.99	-40	500	3.65	-39

Table 3: Thermal conductivities ($W.m^{-1}.K^{-1}$) obtained from experimental measurements of thermal diffusivity using the rear-face flash method on C_1, C_3 and C_{3^*} ceramics between 50 °C and 500 °C under Ar/5 % H_2. Measurements were taken in the pressing direction. The experimental uncertainty is around 3%.

in thermal conductivity with temperature is similar for the three studied ceramics, although their microstructures are very different. Therefore, it seems possible to dissociate the effects of temperature from those of microstructure.

3.3. Limits of the classical correlations for these non-standard UO_2 ceramics

In order to highlight the difference between the thermal behavior of the studied ceramics and that of ceramics produced by the standard process, and thus justify the need to develop a specific model for this type of ceramics, the experimental results are compared with those obtained using the empirical law of Fink (2000). This law, recommended in particular by Carbajo et al. (2001) and more recently by Vlahovic et al. (2018) for the study of the thermal behavior of standard porous UO_2 ceramics, is given by the equation (6) as a function of the normalized temperature t ($t = T(K)/1000$, see above):

$$\lambda_{UO_2,95\%}(T) = \frac{100}{7.5408 + 17.692\,t + 3.6142\,t^2} + \frac{6400}{t^{\frac{5}{2}}}\,e^{-16.35/t} \tag{6}$$

This empirical correlation is based on thermal diffusivity measurements carried out on standard UO_2 ceramics with a total porosity volume fraction (c_T) of the order of 5 %. By correcting for the effect of porosity with a factor F_p, the conductivity of the 100 % dense solid is given by the equation (7).

$$\lambda_{UO_2,100\%}(T) = F_p(T,\,0.05)\;\lambda_{UO_2,95\%}(T) \tag{7}$$

As explained in the introduction, the correction factor recommended by IAEA (2006) is given by the following equation, where c_T is the total porosity volume fraction ($t = T(K)/1000$):

$$F_p(T,\,c_T) = \frac{1}{1 - (2.6 - 0.5\,t)\,c_T} \tag{8}$$

This correction factor takes into account the morphological characteristics of the pores present in standard UO_2 ceramics. Various expressions have been proposed to express the effect of porosity on the conductivity of these ceramics, as a scatter of experimental results has

been observed (Lucuta et al., 1996; Harding and Martin, 1989). As a result, the empirical laws giving the conductivity of 100 % dense UO_2 are associated with a rather large uncertainty, and this is particularly the case for Fink's law corrected for porosity, the uncertainty of which is 10 % between 0 and 1700 °C (Fink, 2000). A more detailed knowledge of the conductivity of 100 % dense UO_2 is therefore a prospect for improving the model. In particular, based on the recent development of numerical methods at very small scales and in particular molecular dynamics, a study of the thermal transport properties of UO_2 at the atomic scale could allow this law to be evaluated numerically (Phillpot et al., 2011; Chen et al., 2014; Kim et al., 2016; Yang et al., 2022). As no such results are available at this stage, in this work we adopt the law (7) to estimate the conductivity of the 100 % dense UO_2 solid at a given temperature.

In order to study the ability of Fink's model to predict the thermal behavior of the UO_2 ceramics under consideration, the correlation (6) has been used by computing the factor F_p for a total volume fraction of porosity equal to that of the ceramics of interest. Figure 5 shows the evolution with temperature of the thermal conductivity of the three ceramics of interest, evaluated experimentally and with Fink's law.

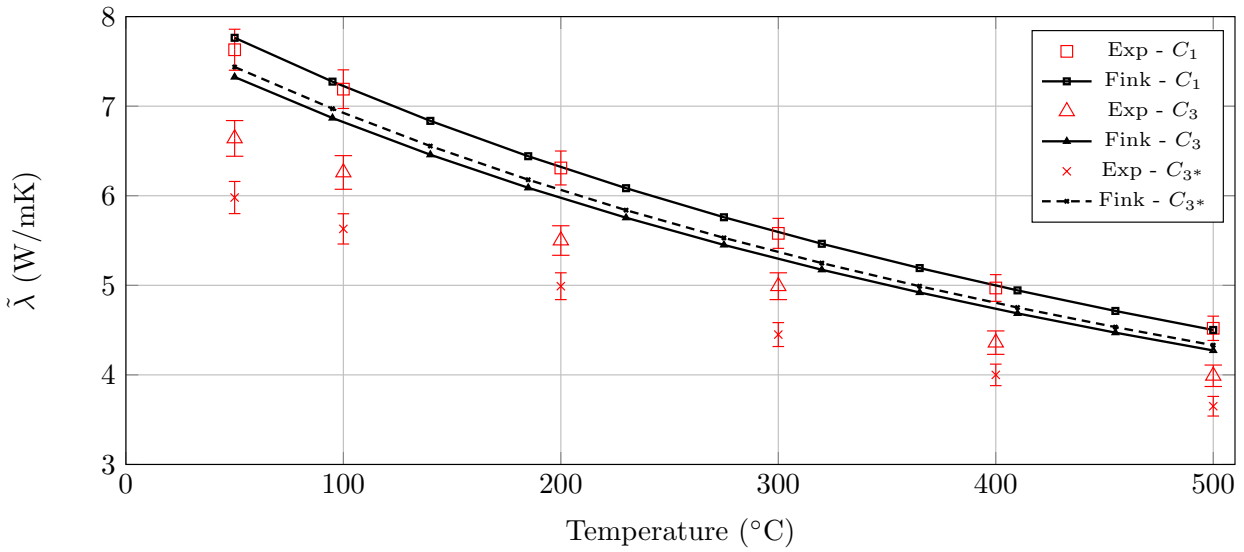

Figure 5: Thermal conductivity measured experimentally and evaluated with the Fink's correlation (6) corrected for porosity for ceramics C_1, C_3 and C_{3*} between 50 and 500 °C (the temperature gradient is prescribed along the pressing direction attached to the fabrication process).

In the case of ceramic (C_1) with the lowest total and open porosities, the thermal conductivity calculated using Fink's law is close to the experimentally measured value. This law therefore appears to be well suited to UO_2 porous ceramics with a low inter-granules porosity. Thus, the thermal behavior of these ceramics approaches that of standard UO_2 ceramics. On the other hand, the differences are marked for the ceramics C_3 and C_{3*}, for which Fink's law leads to a clear overestimation of the thermal conductivity. This confirms that the inter-granules porosity, present in the studied ceramics but not in the standard ceramics, strongly degrades their thermal behavior. This degradation cannot be predicted by standard models such as Fink's law. Furthermore, Fink's law predicts that the thermal conductivity of ceramic C_{3*} is higher than that of ceramic C_3, whereas experimental measurements show

that it is actually much lower. This arises because the porosity correction used in Fink's law depends only on the volume fraction of the total porosity and does not take account of pore shape and orientation. In fact, although ceramic C_{3^*} has a volume fraction of total porosity slightly lower than that of ceramic C_3 (and the same volume fraction of inter-granules porosity), as explained above, the orientation of its inter-granules pores plays a first order role in its thermal conductivity by significantly decreasing it. These experimental results therefore highlight the importance of developing a model that is more representative of the effect of pores, and in particular inter-granules pores, on the thermal behavior of the studied ceramics.

Ceramics produced by the alternative process therefore have very different porosity from those of ceramics obtained by the standard one, which has a direct impact on their thermal behavior. In particular, the presence of inter-granules pores makes the models developed for standard fuels irrelevant for fuels obtained by the alternative process. It is therefore necessary to develop new models for predicting their thermal conductivity that take their microstructural characteristics into account. This is precisely the objective of the following section.

4. A two-scale approach to modeling the effects of pores

As highlighted in the previous section, the studied UO_2 ceramics have complex porosity networks at different scales. In addition, previous comparisons with the Fink's correlation have shown that their respective effects on the thermal behavior of ceramics are also discrepant. Hence, we hypothesize that this discrepancies are due to the porosity. In order to represent the effect of porosity on the thermal behavior of the studied UO_2 ceramics, a two-scale model is proposed which separates the effects of the two porosity families. It is given by the equation (9), where κ_{I-G} and κ_{occ} represent the respective effects of inter-granules and occluded pores, $\tilde{\lambda}$ the effective conductivity and $\lambda_{UO_2,100\%}$ that of 100 % dense UO_2 :

$$\frac{\tilde{\lambda}}{\lambda_{UO_2,100\%}} = \kappa_{I-G}\,\kappa_{occ} \tag{9}$$

This equation is obtained by scale separation as illustrated on figure 6:

- On the small scale, the effect of inter-granules pores is not visible, which means that the matrix conductivity can be defined as the conductivity of the UO_2 degraded by the only presence of the occluded pores ($\tilde{\lambda}_{mat} = \kappa_{occ}\,\lambda_{UO_2}$),
- On the large scale, the effect of occluded pores is only visible on average, which means that the effective conductivity can ultimately be calculated as the degradation of the UO_2 matrix conductivity by the effect of inter-granules pores ($\tilde{\lambda} = \kappa_{I-G}\,\tilde{\lambda}_{mat}$).

As 3D characterizations have shown that the inter-granules network is almost completely interconnected (see Moutin et al. (2024), section 4.3), the contribution of the inter-granules porosity to the volume fraction of closed porosity c_{cl} is neglected. In other words, c_{cl} will hereafter refer to the porosity revealed on the small scale.

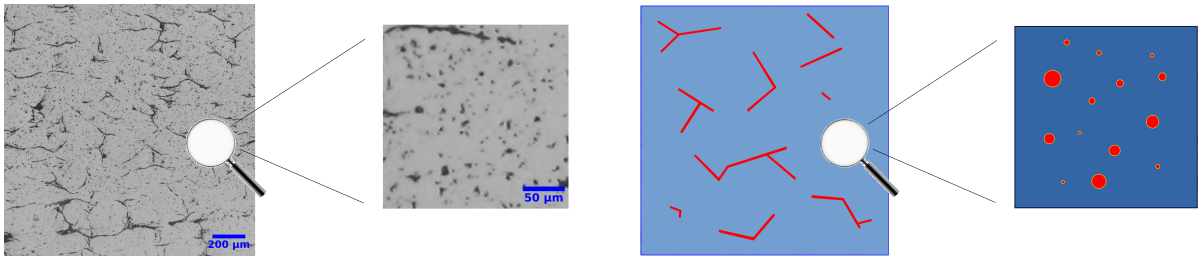

Figure 6: Illustration of the two separated scales in the studied porous ceramics.

4.1. Consideration of the effects of occluded pores

On the small scale, the occluded pores can be seen as a distribution of gaseous spheres homogeneously dispersed in the dense UO_2 solid matrix. Since occluded pores are associated with closed porosity, we assume that the gas contained in these pores is that of the sintering atmosphere, namely dihydrogen. Maxwell's model therefore seems relevant for considering the effects of these pores on the effective properties of ceramics. This model, which is equivalent to one of the two Hashin-Shtrikman bounds in the case of a two-phase medium (Hashin and Shtrikman, 1963), gives a fairly accurate estimate of the effective conductivity $\tilde{\lambda}$ of a heterogeneous medium composed of an isotropic dispersion of spherical inclusions in a matrix (Maxwell, 1873; Torquato and Haslach Jr, 2002).

In our situation, Maxwell's model yields (10) where $\lambda_{UO_{2.100\%}}$ is the thermal conductivity of 100 % dense UO_2, λ_{H_2} is the thermal conductivity of the gas in the occluded pores, c_{cl} is the volume fraction of closed porosity (associated with the occluded porosity).

$$\tilde{\lambda}_{mat}=\lambda_{UO_{2,100\%}}\frac{2\,\lambda_{UO_{2,100\%}}+\lambda_{H_2}+2\,c_{cl}\,(\lambda_{H_2}-\lambda_{UO_{2,100\%}})}{2\,\lambda_{UO_{2,100\%}}+\lambda_{H_2}+c_{cl}\,(\lambda_{UO_{2,100\%}}-\lambda_{H_2})} \tag{10}$$

By neglecting the gas conductivity and doing a limited development to the first order on c_{cl}, equation (10) becomes[4] $\tilde{\lambda}_{mat} \approx \lambda_{UO_{2,100\%}}\left(1-\frac{3}{2}\,c_{cl}\right)$. It should then be pointed out

[4]To derive this simplified expression, (10) is first re-written by dividing the numerator and the denominator of its right-member by $2\,\lambda_{UO_{2,100\%}}$. We obtain:

$$\tilde{\lambda}_{mat} = \lambda_{UO_{2,100\%}}\frac{1+\eta/2+c_{cl}\,(\eta-1)}{1+\eta/2+(c_{cl}/2)\,(1-\eta)}$$

with η the contrast parameter defined by: $\eta = \lambda_{H_2}/\lambda_{UO_{2,100\%}}$. Then, the limit when the gas conductivity vanishes is given by taking the limit when η tends to zero, namely :

$$\lim_{\eta\to 0}\tilde{\lambda}_{mat} = \lambda_{UO_{2,100\%}}\frac{1-c_{cl}}{1+c_{cl}/2}$$

Finally, the denominator in this last expression is expanded as a function of the small parameter c_{cl}:

$$\tilde{\lambda}_{mat} = \lambda_{UO_{2,100\%}}(1-c_{cl})\,(1-c_{cl}/2+(1/2)\,(c_{cl}/2)^2+\ldots)$$

As c_{cl} is small (a few percent), the terms multiplicated by $c_{cl}^2, c_{cl}^3, \ldots$ in the Taylor development can be neglected, namely:

$$\tilde{\lambda}_{mat} \approx \lambda_{UO_{2,100\%}}(1-\frac{3}{2}\,c_{cl})$$

that this equation differs from that recommmended by the IAEA (2006) (namely equations (7) and (8)), which is, to first order and ignoring the effect of temperature ($t = 0$), $\tilde{\lambda}_{mat} = \lambda_{UO_{2,100\%}} (1 - 2.6\, c_{cl})$. This empirical correlation is therefore not consistent with that predicted by Maxwell's model[5]. As Maxwell's model is a reference for the pore distribution considered at this scale, we will use it in the following.

The thermal conductivity of 100 % dense UO_2 is obtained using the equation (7) introduced in the previous section and based on Fink (2000). The thermal conductivity of dihydrogen is given in the Appendix A by the equation (A.2), an equation valid at atmospheric pressure between 0 and 1500 °C.

4.2. Consideration of the effects of inter-granules pores

On the large scale, the effect of inter-granules pores on the thermal behavior of ceramics is difficult to predict since these pores are not uniformly distributed in the solid but along the inter-granules boundary. In addition, they are elongated and can be strongly branched. As a result, the Maxwell model defined above remains an upper bound for the actual behavior of the ceramic, but in practice it remains too far from experience. To estimate the effect of inter-granules pores, we have numerically reproduced, as accurately as possible, Representative Volume Elements (RVEs) of the porous network of the studied ceramics. These RVEs are then used to compute effective properties by full-field computations. The virtual RVEs are obtained by superimposing a Voronoi tessellation modeling the granules joint network with a random dispersion of overlapping spheres, which serve to locate pores at the inter-granules boundary (see Meynard et al. (2022)). These virtual RVEs depend on a limited number of parameters: the grain size of the Voronoi tessellation[6], the diameter and the density of the delimiting spheres. To model the ceramic C_{3^*}, an additional parameter (the aspect ratio) has been introduced and corresponds to the affine transformation applied to the tesselation. This additional parameter allows to model the preferential orientation of the inter-granules pores evidenced in ceramic C_{3*} (see 2.2 and Moutin et al. (2023)). These parameters have been tuned in order to select within our class of models the microstructures that are the most representative of the real ones (the optimal values of these parameters are reported Table 2 in Moutin et al. (2023)). In practice, this optimization process minimizes a cost function based on morphological descriptors computed from the 2D cross-sections and compared to the real ones derived from optical microscopy (see Moutin et al. (2023) for more details).

At the end of this optimization process, we obtain a set of parameters that can be used to generate random virtual RVEs that reproduce some characteristics identified on real microstructures. The C_1 and C_3 microstructures mostly differ in terms of density of spheres (this morphological parameter is denoted d_l in table 2 from Moutin et al. (2023)). As this density is divided by two between C_1 and C_3, the number of intersections between the initialy porous inter-granules network and theses spheres decreases dramatically. As each intersection replaces porous area by a solid bridge, the porous network is much more extended in C_3 in comparison to C_1 (see Figure 7). On the other hand, this parameter is almost identical if

[5]As explained above in Section 3, this correction factor is able to represent the thermal conductivity of a wide variety of porous UO_2 ceramics, but is still not precise enough for the particular situation considered here.

[6]In practice, the cell size is defined as the mean size of the spheres included in the Voronoi cells.

we now compare C_3 with C_{3*}, the elongation in a preferred direction of the porous network obtained for the latter (see Figure 7) being obtained by adjusting the aspect ratio (denoted by $AspR$ in table 2 from Moutin et al. (2023)). The dispersion of thermal properties of these RVE due to their random nature is further discussed in Section 4.3.2. For the ceramics under consideration, illustrative views of the virtual RVEs resulting from this optimization process are reported in Figure 7. These virtual RVEs have been partially assessed in Moutin et al. (2023) by 2D full-field thermal simulations.

As explained in Section 2.1, ceramics C_1 and C_3 have also been imaged in 3D by X-Ray micro-computed (see Figure 3). This 3D visualization of the microstructures of the studied ceramics also enabled us to reveal that inter-granules pores are highly interconnected in 3D (see Moutin (2023) for more details). These observations confirm that inter-granules pores can be assimilated to open porosity. Therefore, the gas they contain is the same as that present in the furnace during the thermal diffusivity measurements, i.e. vacuum, air or helium for the first series of measurements and a mixture of argon and dihydrogen for the second series. The thickness of the inter-granules pores, which had been assumed to be of the order of one micron, was estimated from X-ray tomography images. The fact is that the thickness is rather homogeneous and close to 3 µm. This is the value used to generate the virtual microstructures.

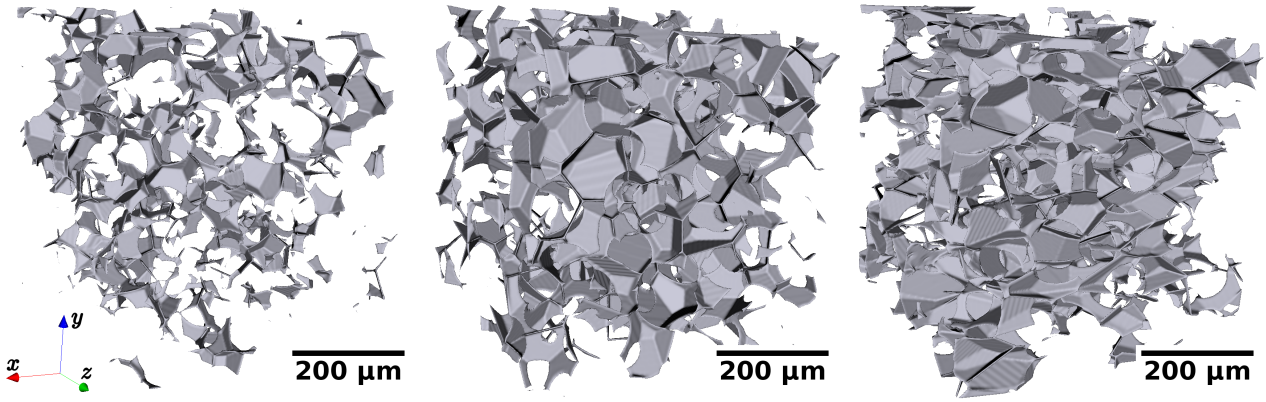

Figure 7: 3D illustrative views of local volumes ($\approx$ 650x650x650 µm^3) on the tuned virtual microstructures associated respectively with the ceramics C_1, C_3 and C_{3*} (left to right) (Moutin et al., 2023).

The laws adopted to model the conductivities of gases with their validity domain are gathered in Appendix A. For the conductivity of helium, we use the equation (A.2). Assuming that the furnace tightness is not perfect, the effect of an air inlet was evaluated by comparing the conductivity of pure helium at 50 °C with that of a helium/air mixture at 95 % helium to study its degradation. The conductivity of the mixture was evaluated using the model proposed by Eckert et al. (1960). This study shows a degradation of the order of 10 % in the thermal conductivity of helium due to the presence of air under the conditions tested. This degradation has little effect on the effective thermal conductivity and is negligible compared to other phenomena that may be involved, in particular the Knudsen effect, which is discussed below (see Section 5.2).

Equations (A.3) and (A.4) are used to calculate air and argon conductivities, respectively. As explained in Section 2.3, to avoid UO_2 oxidation during heating, the measurements are

not carried out under pure argon but under a mixture of argon with 5 % dihydrogen. We show in Appendix B that the addition of dihydrogen has very little effect on the simulated effective conductivity. Consequently, the thermal conductivity law considered for the mixture is that for pure argon.

4.3. Full-field simulation with a Fast-Fourier-Transform (FFT)-based solver

4.3.1. Overview of the method

Our approach relies on numerical homogenization technique, the so-called Representative Volume Element (RVE) method, conceptualized in Hill (1963), and first implemented in the 90s (see, *e.g.* Hazanov and Amieur (1995)). Namely, we impose an averaged thermal gradient $\langle \boldsymbol{\nabla} T \rangle_V$ on a RVE denoted V, and compute the related averaged thermal flux $\langle \boldsymbol{\Phi} \rangle_V$ ($\mathrm{W.m^{-2}}$) by means of a full-field simulation. More precisely, we postulate that the local conductivity is isotropic ($\boldsymbol{\lambda}(\boldsymbol{x}) = \lambda(\boldsymbol{x})\, \boldsymbol{I}$ with $\boldsymbol{I}$ the identity second-order tensor). Then, the full-field simulation amounts to solving numerically the following partial differential equation

$$\begin{cases} \boldsymbol{\nabla} \,.\, \boldsymbol{\Phi}(\boldsymbol{x}) = 0 \\ \boldsymbol{\Phi}(\boldsymbol{x}) = -\lambda(x) \nabla T(\boldsymbol{x}) \\ T(\boldsymbol{x}) = T^*(\boldsymbol{x}) + \boldsymbol{u} \cdot \boldsymbol{x} \end{cases} \tag{11}$$

for given directions $\boldsymbol{u} = \langle \boldsymbol{\nabla} T \rangle_V$, subjected to some boundary conditions[7].In Equations (11) above, the temperature have been decomposed into a linear part and an unknown periodic function T^* of vanishing average. Last, we approximate the effective conductivity along the direction $\boldsymbol{u}$ by the apparent conductivity

$$\tilde{\lambda}_{\boldsymbol{u}} = -\frac{\langle \boldsymbol{\Phi}_{\boldsymbol{u}} \rangle_V}{\langle \boldsymbol{\nabla}_{\boldsymbol{u}} T \rangle_V}. \tag{12}$$

Notice that $\tilde{\lambda}_{\boldsymbol{u}}$ is a random variable since the microstructure itself is random, and implicitly depends on the size L of V. We will study the latter dependence before choosing a sufficiently large L in Section 4.3.2.

This method was shown to converge almost-surely to the actual effective conductivity when the RVE size goes to infinity (see Bourgeat and Piatnitski (2004)). This results holds for various boundary conditions (Dirichlet, Neumann or periodic). Nevertheless, as was suggested by numerical experiences in various contributions (see Kanit et al. (2003) or Schneider et al. (2022)) and recently established mathematically in a restricted framework (see Clozeau et al. (2023)), periodic boundary conditions (altogether with a periodic microstructure) prove superior in terms of convergence rate. Naturally, this applies only to microstructures that are ergodic, stationary, with finite range of dependence, and for which a suitable periodization can be built[8].

[7]In the next computations of the effective conductivity at a given temperature $T_0 \in [50°C\,;\, 2000°C]$, the temperature gradient $\boldsymbol{u}$ imposed in the FFT simulations is chosen to be small enough to consider that the conductivities of the solid and the gas are constant and equal to their values at T_0 throughout the RVE.

[8]This periodization should be compatible with the statistics in the sense that it should preserve the stationarity property; see Clozeau et al. (2023) and Schneider et al. (2022).

From a numerical perspective, solving (11) remains challenging, since large RVEs are sought for because their apparent properties enjoy lower variances and biases. Simultaneously, the discretization step should be smaller than the finest features of the microstructure to preserve the numerical accuracy. When it comes to solvers, two main classes are of common use: Finite Element Solvers (not discussed here) and FFT-based solvers. Introduced in Moulinec and Suquet (1994), the latter are quite popular in micromechanics, for two main reasons, besides their simplicity (see Brisard and Dormieux (2010)):

1. Relying on efficient parallel implementations of the FFT (see for example AMITEX-FFTP Gélébart and Mondon-Cancel (2013)), they can tackle very large number of degrees of freedom, leading to large RVE sizes,

2. The discretization involves a regular cartesian grid inside a cube (a voxel grid), far simpler to build than classical tetraedric meshes. Also, periodic boundary conditions are the more natural ones once a periodic microstructure can be produced.

We refer the reader to the recent review Schneider (2021) and to the online course Brisard et al. (2022) for a broad overview of the method and its developpments.

4.3.2. Numerical setup

The microstructures have been produced with version 1.0 of the Mérope software (see Josien (2024) and `https://github.com/MarcJos/Merope`) while FFT computations are performed with version 1.8 of the TMFFT software (components of the PLEIADES platform), respectively. As explained above, the simulations are performed on periodic cubic cells that are regular grids of voxels. The size of the cells, represented by the width of the cube (L, vox), is an important parameter in the calculation. It must be large enough so that cells are RVEs, but must remain reasonable because FFT simulations are expensive in terms of time and memory. Figure 8 shows the evolution of the effective conductivity normalized by the conductivity of the solid obtained for a virtual RVE (associated with the ceramic C_3) as a function of the cell size (L). Here insulated pores are considered (conductivity is taken as equal to $10^{-6}\,\mathrm{W.m^{-1}.K^{-1}}$) while the conductivity of the solid is arbitrarily set equal to that of the dense UO_2 at 50 °C. By maximizing the constrast between the conductivity of the bulk and that of the pores, we are studying the most penalizing situation with regard to the role of the porous network on the thermal behavior of ceramics. For a given cell size, it should be borne in mind that the generated porous network is the result of a random process. Therefore, the positions of the centres of the Voronoi cells and of the delimiting spheres will change from one sample to another.

As a result (see Figure 8), the computed effective conductivity varies for a given cell size. We observe that both the uncertainty and the bias decrease rapidly with L and become small above $L = 2^9 = 512$ vox (corresponding to 778 µm), namely $< 1\%$ and $< 0.5\%$ of relative error, respectively. The effective conductivity finally obtained is averaged over 5 simulations carried out on independent virtual microstructures, thus guaranteeing a good representativeness of the average value, namely a relative error of 1% with a 95% confidence interval. We also checked the effect of grid refinement on the simulated effective conductivity on a smaller RVE –for various gaseous environments. If the number of voxels per porosity thickness is increased by two, the induced relative error on the apparent conductivity does

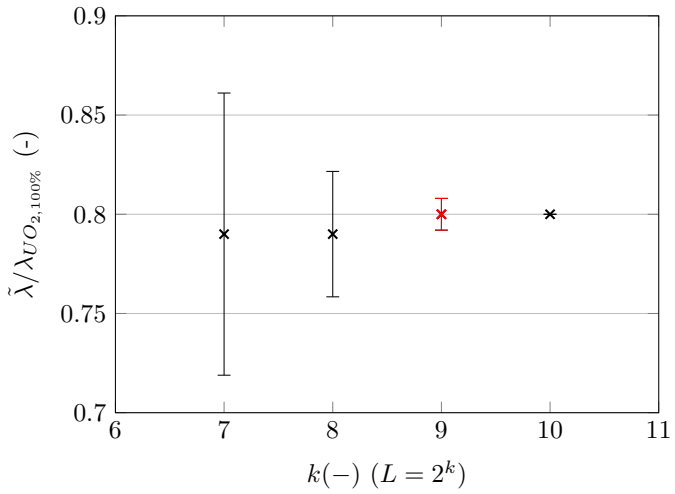

Figure 8: Evolution of normalized effective conductivity as a function of RVE size (L) and uncertainties associated with the random process of virtual microstructure generation (insulated pores are considered (10^{-6} W.m^{-1}.K^{-1}) while the conductivity of the solid is arbitrarily set equal to that of the dense UO_2 at 50 °C).

not exceed 2%. As a conclusion, for our choice, taking into account all aforementioned sources of numerical errors, we end up with an error of approximately 3% on the effective conductivities, with a 95% confidence interval. (Notice that this value is the same as the experimental uncertainty.) As a consequence, we will consider as negligible phenomena which have an influence on the effective thermal conductivity of less than 3%.

The aforementioned value of RVE size and the related discretization steps will be used for the numerical simulations. For this cell size, using Mérope then TMFFT, the memory usage is of the order of 15 GB. The cell generation time is of the order of one minute with Mérope, and the computation time is of the order of one hour on 32 CPUs with TMFFT (for a calculation in the three spatial directions).

4.4. Conclusion: main ingredients of the proposed model

For a given microstructure C_1, C_3 or C_{3*} and experimental conditions defined by the prescribed temperature T and the nature of the gas in the furnace, the effective conductivity is computed as follows :

i) The conductivity $\tilde{\lambda}_{mat}(T)$ is computed by using relations (10), $\lambda_{UO_{2,100\%}}(T)$ and $\lambda_{H_2}(T)$ being given by (7) and (A.2), respectively. In (10), c_{cl} is reported in table 1 for the considered microstructure. See Section 4.1 for additional details on this step.

ii) A RVE of the considered microstructure is generated by superimposing two elementary random sets (a Voronoi tesselation and a dispersion of overlapping spheres). The resulting random set is defined by the grain size of the Voronoi tesselation as well as the diameter and the density of the spheres dispersion. These parameters are defined for each microstructure C_1, C_3 and C_{3*} in Moutin et al. (2023), Table 2. See Section 4.2 for additionals details on this step.

iii) For this RVE sample, the effective conductivity is computed by FFT-based solver where $\tilde{\lambda}_{mat}(T)$ is defined in i) above while the conductivity of the inter-granules porosity is given by one of the relations reported in Appendix A depending on the surrounding gas in the furnace. See Section 4.3 for additional details on this step.

In addition, it is worth empasizing that:

Remark 1. *The effective conductivity does depend on the RVE sample issued from step iii). As explained in Section 4.3.2, steps ii) and iii) are repeated for five different realizations of the same random microstructure, the final effective conductivity being the average of the five estimations of the effective conductivities. This averaging operation ensures that choosing five other realisations will lead to an effective conductivity value that is very close to the simulation results that will be presented in the next section (deviation of* 1 % *with a* 95% *confidence interval, see above).*

Remark 2. *The effect of inter-granules pores is here derived by simulations of RVE of models of microstructures which means that the inter-granules pore effect is not provided by an analytical law. Work is underway to determine analytical correlations as a function of contrast and microstructure.*

Finally, the proposed model for κ_{I-G} is plotted against the IAEA correlation in Figure 9 for the three different ceramics. Here, insulated pores are considered. The particular shape of the inter-granules pores forms thermal barriers which significantly degrade the thermal conductivity of the solid. This degradation increases with the extension of the porous network if we compare the microstructures C_1 and C_{3*}. The even greater degradation obtained for C_{3*} when compared with C_3 is related to its anisotropy: there are just as many barriers in these two microstructures, but in the case of C_{3*}, these barriers are preferentially oriented perpendicular to the heat flow. As the IAEA model is not adapted to this type of shape and distribution of pores, it underestimates this degradation.

5. Discussion

Before going any further, it is important to emphasize that the model presented in the previous section and now used to discuss the experimental trends reported in Section 3 has not undergone any particular recalibration. It depends only on the considered microstructures through:

- The volume fraction of occluded pores c_{cl} as reported in table 1;
- The virtual RVEs of the three ceramics, see Figure 7;
- The average thickness of the inter-granules pore network, 3 µm;

as well as, for a given temperature:

- The conductivity law of the 100 % dense UO_2 (relation (7)) ;
- The conductivity law of the dihydrogen gas contained in the occluded pores (relation (A.2));

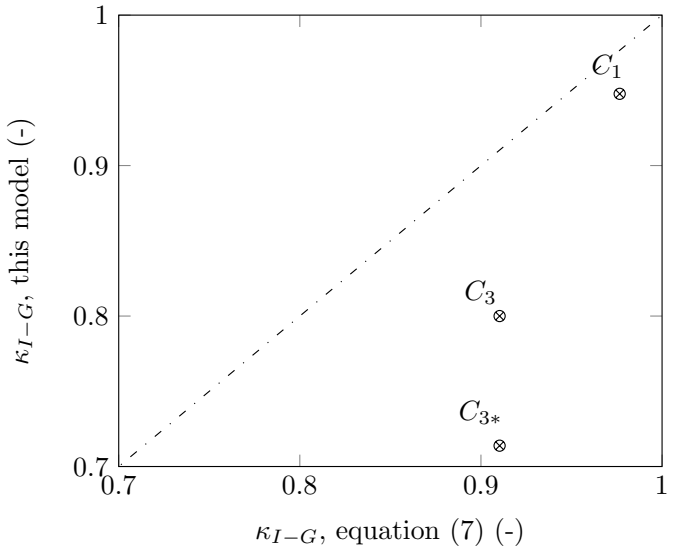

Figure 9: Degradation of the matrix conductivity by the effect of the inter-granules pores κ_{I-G}: the predictions of the proposed model are compared to the ones provided by IAEA correlation (equations (7) and (8)) for the three ceramics under consideration, C_1, C_3 and C_{3*}.

- The conductivity law of the gas contained in the inter-granules porosity (open porosity) which will depend on the gas present in the furnace : relation (A.2) for helium, (A.3) for air and (A.4) for argon.

5.1. Effect of the inter-granules porosity (measurements at 50 °C in vacuum)

Figure 10 shows the results obtained experimentally and with the model on the three ceramics of interest at 50 °C in vacuum. Remarkably, the model reproduces well the thermal behavior evaluated experimentally in vacuum for the three ceramics of interest. The numerical result is within the experimental and the numerical uncertainties, which are both of order of 3 %. The differences in the thermal behavior of the three ceramics are well reflected, which is particularly interesting for the C_{3^*} ceramic, whose inter-granules pores have a preferential orientation perpendicular to the measurement direction.

5.2. Knudsen phenomenon (effect of the gaseous environment at 50 °C)

As shown in Figure 10-left, the discrepancies between the model and the experimental measurements are the largeest for helium. In fact, the model predicts a significant effect of the gas in the pores, whereas this effect appears to be very small experimentally. The preferred hypothesis to explain this weak effect of the gas in the inter-granules pores is the Knudsen effect, also known as the "Smoluchowski" effect (Litovsky et al., 2005; Calvet et al., 2022). This phenomenon occurs when the mean free path of the gas molecules contained in the pores becomes non-negligible compared to the size of these pores. Heat transfer in the pores, which is governed by collisions between the gas molecules, is then degraded because the gas molecules come into contact with the solid, which limits the collisions between them. For a given pore size, this Knudsen effect is all the more pronounced as the mean free path of the molecules of the gas in question is large, which is particularly the case for helium. This

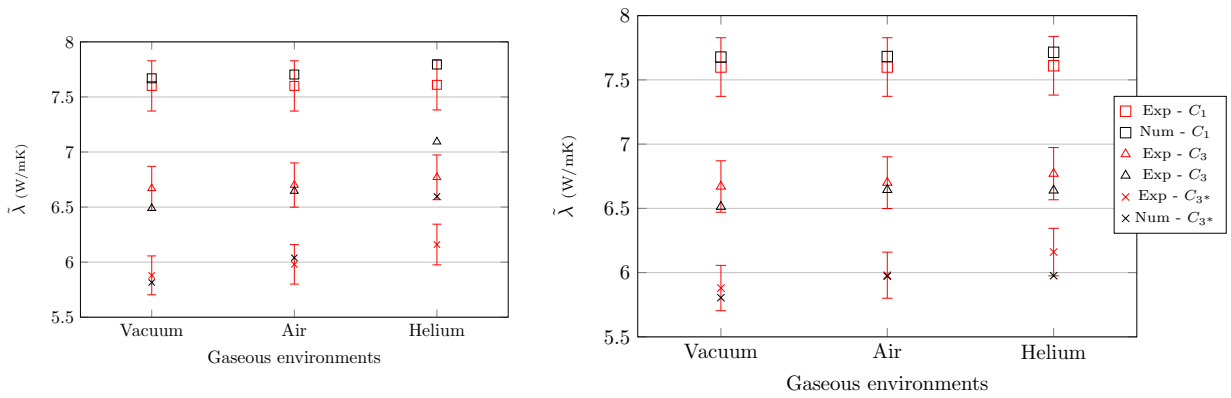

Figure 10: Thermal conductivity measured experimentally (in red) and simulated numerically (in black) on ceramics C_1, C_3 and C_{3^*} at 50 °C in different gaseous environments without (left) and with (right) consideration of the Knudsen effect (the temperature gradient is prescribed along the pressing direction attached to the fabrication process). Uncertainties for simulated results equal those on experimental measurement, namely 3% (see 4.3.2).

property would bring the conductivity of helium closer to that of air under the conditions studied. Moreover, this phenomenon is particularly important when the pore thickness (e_P) is small and the pressure (P) is low, which corresponds to the conditions studied ($e_P \approx 3$ µm and $P = P_{atm}$).

Therefore, the mean free path reads:

$$\delta_0 = \frac{k_b T}{\sqrt{2}\pi d_m^2 P} \tag{13}$$

where k_b ($\mathrm{m^2.kg.s^{-2}.K^{-1}}$) is the Boltzmann constant and d_m (m) is the molecular diameter of the gas particles while the Knudsen number denoted by K_n is the ratio between this mean free path of the gas molecules and the pore thickness, $K_n = \delta_0 \,/\, e_P$. Following Moscardini et al. (2018), the degradation of the thermal conductivity of a gas by the Knudsen effect is given by the following correlation:

$$\lambda(K_n) = \frac{\lambda}{1 + 2\,\beta\,K_n} \tag{14}$$

In this expression, β is defined by:

$$\beta = \frac{2 - \alpha_c}{\alpha_c} \quad \text{and} \quad \alpha_c = \frac{2.4\,m_r}{(1 + m_r)^2} \tag{15}$$

with $m_r = m_g/m_s$ the ratio of the gas (m_g) to the solid (m_s) atomic masses. It is clear that the degradation of conductivity increases with the mean free path δ_0 and decreases with the inter-granules pore thickness e_P but also with the pressure P. Table 4 shows the different molecular diameter values used for the gases studied (at 50 °C, $P = 1$ atm and $e_P = 3$ µm). The Knudsen numbers as predicted by Relation (14), which involves the mean free path defined by (13) are also compared in this Table for the different possible gases. As a result of the larger mean free path of helium, a much stronger Knudsen effect is expected for this gas.

Gas	Air	Argon	Helium
d_m $(10^{-10}m)$	3.64	3.58	2.58
K_n $(-)$	2493	2577	4963

Table 4: Molecular diameters (d_m) and Knudsen number (K_n, at 50 °C, $P = 1$ atm and $e_P = 3$ µm) used for the different gases studied in Sections 5.2 and 5.3.

Figure 11 shows the thermal conductivities of helium and air at 50 °C as a function of pore thickness with and without the Knudsen effect. As expected, the thermal conductivity of helium is significantly degraded while that of air is only slightly modified. Thus, for the inter-granules pore thickness considered (of the order of 3 µm), the thermal conductivity of the two gases is close. The Knudsen effect therefore justifies the small differences observed experimentally in the different gas environments.

Figure 11 also shows the degradation in thermal conductivity observed with the model when the Knudsen effect is taken into account when simulating the behavior of the three ceramics of interest in the different gaseous environments. As expected, when the Knudsen effect is taken into account, the effective thermal conductivity simulated in the case where the inter-granules pores are filled with helium is significantly degraded[9]. The numerical results are therefore in good agreement with the experimental measurements within the experimental and the numerical uncertainties in the three gaseous environments tested (see Figure 10).

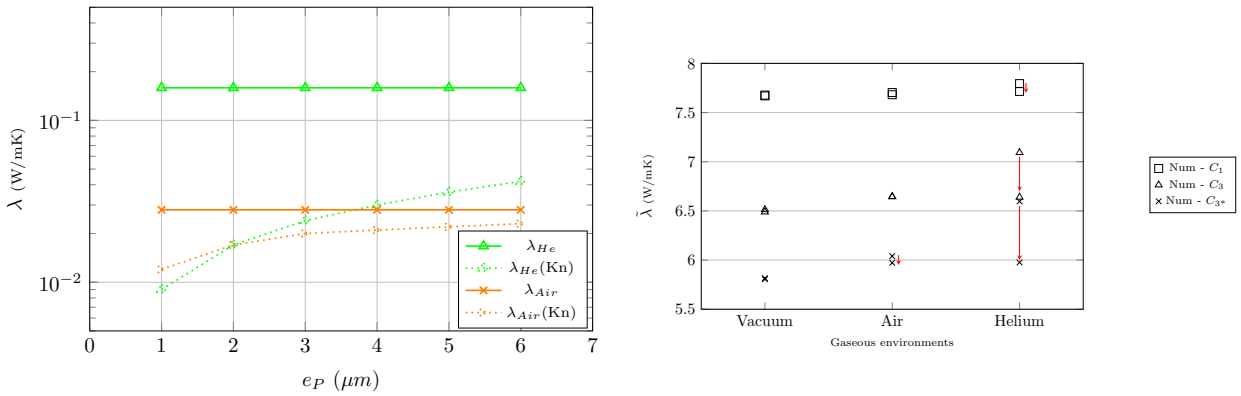

Figure 11: Evolution of the thermal conductivity of helium and air as a function of pore thickness with and without consideration of the Knudsen effect (left) and the consequences for the effective conductivity simulated with a pore thickness of 3 µm (right).

Given the strong influence of the Knudsen effect on the thermal conductivity of the gas contained in the inter-granules pores, which have a thickness of 3 µm, it is reasonable to assume that the thermal conductivity of the gas in the occluded pores, which are present on a small scale, must be even more strongly degraded by this effect. In practice and as the gas conductivity remains low compared to that of the dense ceramic, it appears that the thermal conductivity of the gas present in the occluded pores has very little influence on the

[9]For helium in C_3* ceramics, this effect changes the value $\tilde{\lambda}$ by 10%, which is much larger than the numerical uncertainty of 3%, *cf.* Figure 11, compared with Section 4.3.

thermal conductivity of the matrix. Indeed, according to equation (10), for a ceramic with an occluded pore volume fraction of 2 %, a degradation of the matrix conductivity of only 0.1 % is expected when the thermal conductivity of the gas present in these pores (dihydrogen) is replaced by that of a vacuum.

Thus, the model gives a good prediction of the thermal behavior at 50 °C of the different studied ceramics, as well as the effect of the gaseous environment. The Knudsen effect plays an important role in the thermal behavior evaluated in a helium environment and justifies the weak influence of the environment on the thermal conductivity observed experimentally.

5.3. Effect of temperature including radiative contribution (measurements up to 500 °C under an argon with 5 % dihydrogen atmosphere)

At higher temperatures, in addition to the Knudsen effect mentioned above, which reduces conductivity, heat transfer by radiation must also be considered. This radiative effect helps to improve the heat transfer properties in the pores and depends very much on the temperature, according to the Stefan-Boltzmann law, which relates that the power per unit area ϕ emitted by a grey body with is surface temperature T through

$$\phi = \epsilon_r \, \sigma \, T^4$$

where ϵ_r (-) corresponds to the emissivity and σ (kg. $K^{-4}.s^{-3}$) is the Stefan-Boltzmann constant. In the studied case, given the morphology of the inter-granules pores, the heat transfer can be described schematically as a transfer between two infinite plates separated by a distance e_P (e_P corresponds here to the thickness of the inter-granules pores, which, as a reminder, is fixed in the model at 3 µm). The net heat flux ϕ_{net} between two facing plates at temperatures T_1 and T_2 can be described from the Stefan-Boltzmann law by the equation (16) (Lienhard IV and Lienhard V, 2017).

$$\phi_{net} = \epsilon_r \, \sigma \, (T_1^4 - T_2^4) \tag{16}$$

Imura and Takegoshi (1974) introduced the idea of associating radiative heat transfer with an improvement in the conduction properties of the medium. In this context, starting from the equation (16), the increase in the thermal conductivity of the gas (λ_g) due to the radiative effect is given by[10]:

$$\lambda(Rad) = \lambda_g + e_P \; 4 \, \epsilon_r \, \sigma \, T^3 \tag{17}$$

The adopted emissivity value for UO_2 is 0.87. The influence of the Knudsen and radiative effects on the thermal conductivity of the argon filling the inter-granules pores as a function of temperature is shown in Figure 12. As a reminder, the conductivity of pure argon is considered rather than that of the Ar/H_2 mixture present in the furnace, since the presence of dihydrogen has very little effect in the proportions considered (see Appendix B).

[10]Equation (17) is derived from equation (16) by using the fact that the difference between T_1 and T_2 is negligible compared to T_1, which gives to the first order the equation: $T_1^4 - T_2^4 = (T_1^2 - T_2^2)\,(T_1^2 + T_2^2) \approx 4T_1^3\,(T_1 - T_2)$. Then, the Fourier's law (equation (1)), which relates the conductivity to the heat flux, is used to derive the additional term in (17).

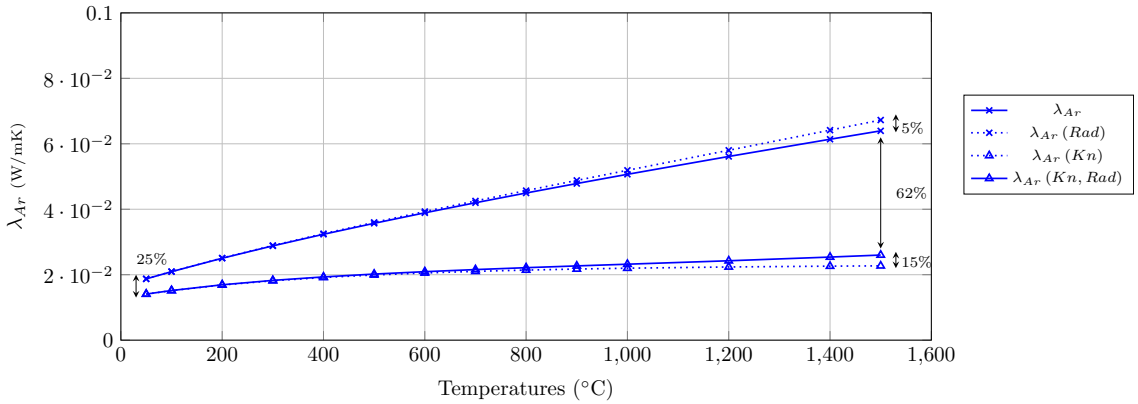

Figure 12: Evolution of the thermal conductivity of argon (λ_{Ar}) as a function of temperature, obtained by considering the radiative effect ($\lambda_{Ar}(Rad)$), the Knudsen effect ($\lambda_{Ar}(Kn)$) and the two coupled effects ($\lambda_{Ar}(Kn, Rad)$).

The radiative effect is negligible in the temperature range of interest (between 0 and 500 °C) and remains very small at higher temperatures. In fact, a 15 % increase in conductivity of the gas is estimated at 1500 °C in the worst case, i.e. including the Knudsen effect. This is due to the small thickness of the inter-granules pores, on which the contribution of radiative transfer to conductivity is directly dependent (see equation (17)). The radiative effect is therefore not considered here. The Knudsen effect plays an important role in gas conductivity. It has already been shown in Section 5.2 that the degradation of thermal conductivity due to this effect is non-negligible at 50 °C, and it appears that this degradation becomes increasingly significant with temperature. The strong dependence of this phenomenon on temperature is due to the mean free path of the gas molecules (see equation (13)). This effect must therefore be taken into account in the simulations carried out.

Figure 13 shows the evolution of the experimentally measured and numerically simulated thermal conductivities as a function of temperature for the three ceramics of interest. The different thermal behaviors observed at 50 °C for the three ceramics are well reflected in the temperature range up to 500 °C. The numerical results are in good agreement with the experimental measurements, being within the experimental and the numerical uncertainties (which are both of order 3 %). The model therefore accurately reproduces the effect of temperature on the thermal behavior of the model ceramics in the temperature range studied.

5.4. Extrapolation up to 2000 °C under an argon with 5 % dihydrogen atmosphere

Finally, the model can be used to study the thermal behavior of the ceramics of interest at temperatures that are difficult to reach experimentally. As an example, Figure 14 shows, for the three studied ceramics, the effective thermal conductivity obtained with the model up to 2000 °C (argon with 5 % dihydrogen atmosphere). This figure also shows the effective conductivities obtained by taking into account the radiative effect, which, as a reminder, depends strongly on the temperature (in T^3). These results show that, even at higher temperatures, the radiative effect has a negligible impact on the calculated effective thermal properties. To interpret this extrapolation correctly, it is important to bear in mind that the model has only been experimentally validated up to 500 °C, but it is also important to be aware of

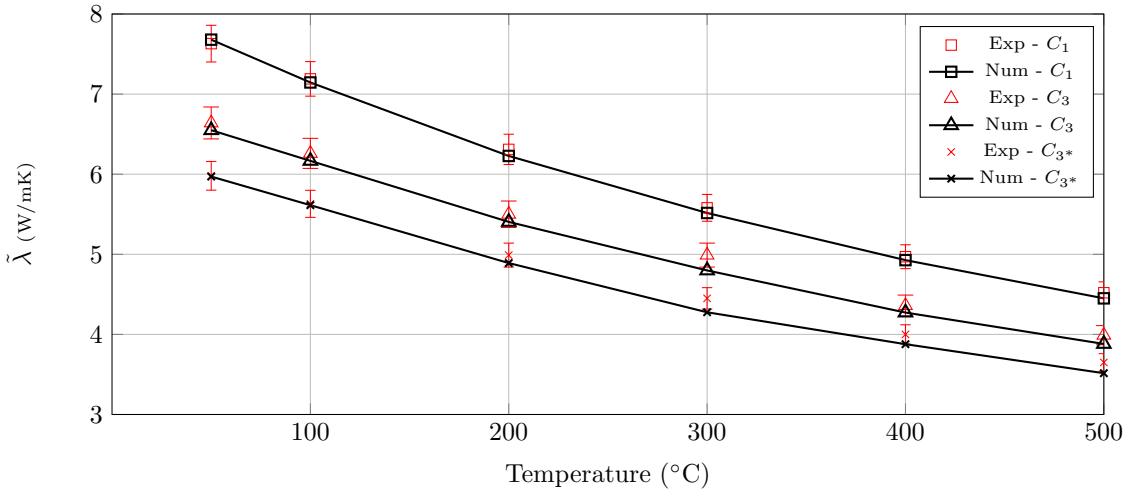

Figure 13: Experimentally measured (red) and numerically simulated (black) thermal conductivities of ceramics C_1, C_3 and C_{3*} between 50 and 500 °C under an argon with 5 % dihydrogen atmosphere (the temperature gradient is prescribed along the pressing direction attached to the fabrication process). Uncertainties for simulated results equal those on experimental measurement, namely 3% (see 4.3.2).

the ranges of validity of the various laws used. In particular, the relationship (A.2), which gives the evolution of the conductivity of the dihydrogen contained in the occluded pores with temperature, is only valid up to 1500 °C. Given that the studied ceramics have little occluded porosity and that its effect is small, few differences are expected. More importantly, the uncertainty associated with the law (6) used to determine the conductivity of dense UO_2 increases from 10 to 20 % above 1700 °C. Our analysis suggests that this uncertainty becomes predominant in our model.

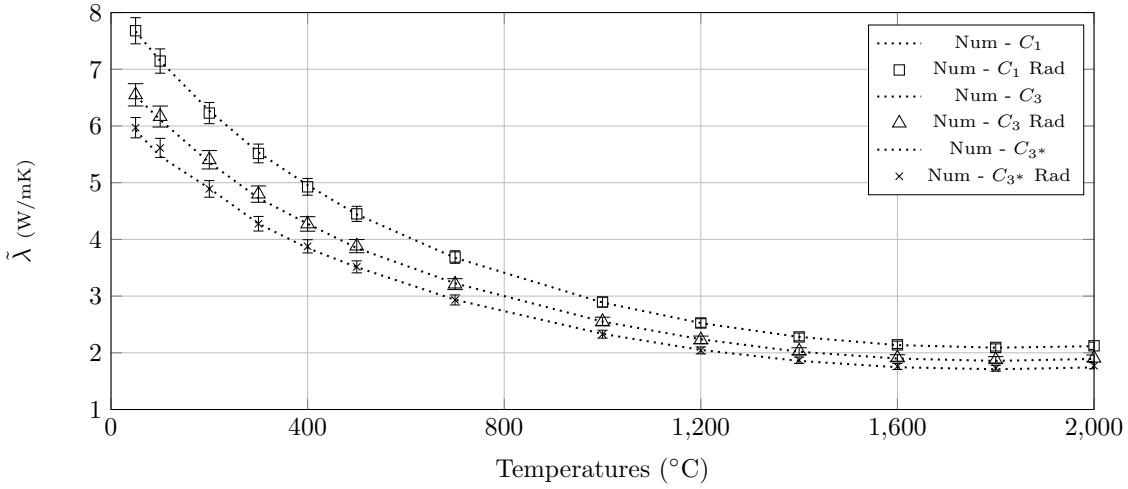

Figure 14: Thermal conductivities numerically simulated for ceramics C_1, C_3 and C_{3*} up to 2000 °C under an argon with 5 % dihydrogen atmosphere (the temperature gradient is prescribed along the pressing direction attached to the fabrication process).

These simulations highlight the strong interest of developing a faithful model to study the properties of materials under conditions that are difficult to access experimentally.

6. Conclusions and future works

Experimental measurements of thermal diffusivity have been carried out on three UO_2 ceramics (C_1, C_3 and C_{3^*}) which differ in their open and closed porosity volume fractions and also in the anisotropic microstructure of the C_{3^*} ceramic. Two sets of experimental measurements have been carried out. The thermal diffusivity of the ceramics was first measured at 50 °C in three gaseous environments (vacuum, air and helium) and then between 50 and 500 °C under Ar/H_2. Marked differences in the thermal behavior of the three ceramics of interest were observed which show the potential significant effect of the inter-granules pores on the effective conductivity. As expected, these marked differences are not reproduced by classical correlations for standard UO_2, which do not distinguish between open and closed porosity. Hence, these differences underline the need to accurately characterize the effect of the geometry of porosity on the thermal behavior of such ceramics. This is particularly the case for our C_3 and C_{3^*} ceramics, which are difficult to distinguish by their open and closed porosity volume fractions, but have different thermal conductivities at low and high temperatures (up to 500 °C). Furthermore and more surprisingly at first glance, a very low dependence of the thermal conductivity on the gaseous environment was observed, even for the most porous ceramics.

To take into account the effect of the porosity geometry on the thermal behavior of these UO_2 ceramics, a two-scale model has been proposed. This model dissociates the effects of small scale occluded pores from those of large scale inter-granules pores. The effect of occluded pores on thermal behavior is assessed using the Maxwell model, which gives an accurate estimate of the conductivity of a medium composed of spherical inclusions dispersed in a matrix. These pores are associated with closed porosity and are therefore assumed to be filled with the ceramic sintering gas, i.e. dihydrogen. The effect of inter-granules pores is evaluated by performing numerical simulations using a FFT-based solver on 3D virtual RVEs generated by the optimization process described in Moutin et al. (2023). These pores are considered to be interconnected, which is consistent with observations by tomography (Moutin, 2023), and are therefore associated with open porosity. They are then filled by the gas present in the furnace during the measurements (vacuum, air, helium and argon).

Finally, the model's predictions were compared with the experimental results. The first results were not fully satisfactory with regards to the effect of the gaseous environment at 50 °C. This prompted us to appeal to a more refined model, where we took into account the Knudsen effect, accounting for the mean free path of the gas particles. This effect could not indeed be overlooked because of the low pore thickness, especially for the integranular pores. On the contrary, the conductivity of the matrix is not very sensitive to that of the gas filling the occluded porosity. In other words, occluded pores might be filled with another gas than dihydrogen without affecting much our results. Last, using this more refined model, our numerical experiments were shown to be in good agreement with all the experimental data. The introduction of the Knudsen effect thus might explain the low dependence on the gas environment of the experimental results. We also established that the radiative effect was negligible under the conditions studied.

The study of irradiation effects as well as the simulation of additional physical properties like elastic moduli or permeability are now in progress. From a broader perspective, we aim at a finer knowledge of the relationship between the microstructural characteristics of

interconnected porous ceramics and their physical properties. This will have two beneficial applications. First, this will allow for optimizing the manufacturing protocol, driving it by the desired physical properties. Second, substituting insulated pores at the inter-granules boundary considered in this work by high-conducting (metallic) materials will enable us to assess the improved thermal conductivity of enhanced accident tolerant fuels (such as micro-cell UO_2–Mo pellet Kim et al. (2015)).

Acknowledgments

The authors are grateful for the financial support provided by the CEA and École des Ponts ParisTech via Grant 5765. Many thanks to Mathias Soulon from CEA, who carried out the thermal diffusivity measurements and to Joane Meynard for her initial contribution to this work. The authors are also grateful to Vincent Bouineau from CEA with whom we had fruitful exchanges on this work.

Appendix A. The thermal conductivities of the different gases as a function of the temperature

Here are given the thermal conductivities ($W.m^{-1}.K^{-1}$) of the different gases considered in this work as a function of the temperature T in Kelvin. Therefore, the thermal conductivity of dihydrogen is given by :

$$\begin{aligned}\lambda_{H_2} = (&1.02672 + 0.74409\,T - 4.5470\times10^{-4}\,T^2 - 3.70833\times10^{-9}\,T^3 \\ &+2.67329\times10^{-10}\,T^4 - 1.06021\times10^{-13}\,T^5)\times10^{-3}\end{aligned} \tag{A.1}$$

This law, recommended by Le Neindre (1998), is valid at atmospheric pressure between 0 and 1500 °C. For the conductivity of helium, we use the equation :

$$\lambda_{He} = 0.0476 + 0.362\times10^{-3}\,T - 0.618\times10^{-7}\,T^2 + 0.718\times10^{-11}\,T^3 \tag{A.2}$$

proposed by Drut (1968) and in good agreement with that given by Le Neindre (1998) (differences < 3 % in the temperature range in question).

As proposed by Stephan and Laesecke (1985) the following relation is used to evaluate the conductivity of air :

$$\lambda_{Air} = -3.9333\times10^{-4} + 1.0184\times10^{-4}\,T - 4.857\times10^{-8}\,T^2 + 1.5207\times10^{-11}\,T^3 \tag{A.3}$$

This equation is also in good agreement with that proposed by Le Neindre (1998) (differences lower than 1 % in the targeted temperature range). For argon, the conductivity is given by :

$$\lambda_{Ar} = \left(7.8\,T^{0.3} + 4.75\,T^{-1} - 30.4 + 1.14\times10^{-2}\,T\right)\times10^{-3} \tag{A.4}$$

relation given by Le Neindre (1998) and valid between 90 et 6000 K.

The predictions of these different laws are reported as a function of temperature in Figure A.15

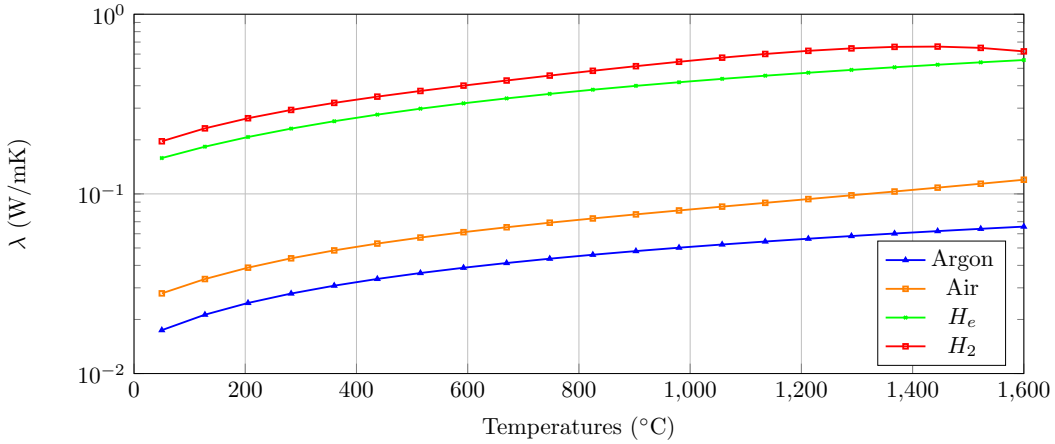

Figure A.15: Evolutions of the thermal conductivity of argon, air, dihydrogen and helium as a function of temperature.

Appendix B. The thermal conductivity of an argon/dihydrogen mixture and its effect on the conductivity of ceramics of interest

The law giving the evolution of the thermal conductivity of the argon/dihydrogen gas mixture at 38 °C as a function of the argon fraction is taken from Srivastava and Srivastava (2004) and plotted in Figure B.16. This law is in good agreement with the other results found in the literature, and in particular those given in Cauwenbergh and Van Dael (1971) for this gas mixture. It should first be noted that argon and dihydrogen have significantly different thermal conductivities, argon being ten times more conductive than dihydrogen. The law of mixing predicts that 10 % dihydrogen will give a conductivity 45 % greater than that of pure argon. However, this increase in conductivity has little effect on the actual behavior of the studied ceramics. In fact, under these conditions, for the C_{3*} ceramic, which is the most porous and therefore the one most affected by changes in gas conductivity in the pores, considering an Ar/H_2 mixture with 90 % argon leads to an increase in effective conductivity of the order of 2 %. The consideration of a gas mixture with 95 % argon is therefore of little interest in this study.

The evolution of the thermal conductivity of argon, dihydrogen and the mixture as a function of temperature was also studied to verify that the conclusions drawn at 38 °C remain valid with increasing temperature. For this purpose, the results obtained by the model given in Papari et al. (2005), which predicts the evolution with temperature of the transport properties of a 50-50 % mixture of argon and dihydrogen, are plotted in Figure B.17. This figure also shows the evolution with temperature of the conductivities of argon and dihydrogen obtained from the equations A.4 and A.2 respectively. It is clear that the evolution of the conductivity of the two gases and that of the mixture are proportional. The effect of temperature can therefore be dissociated from that of the mixture.

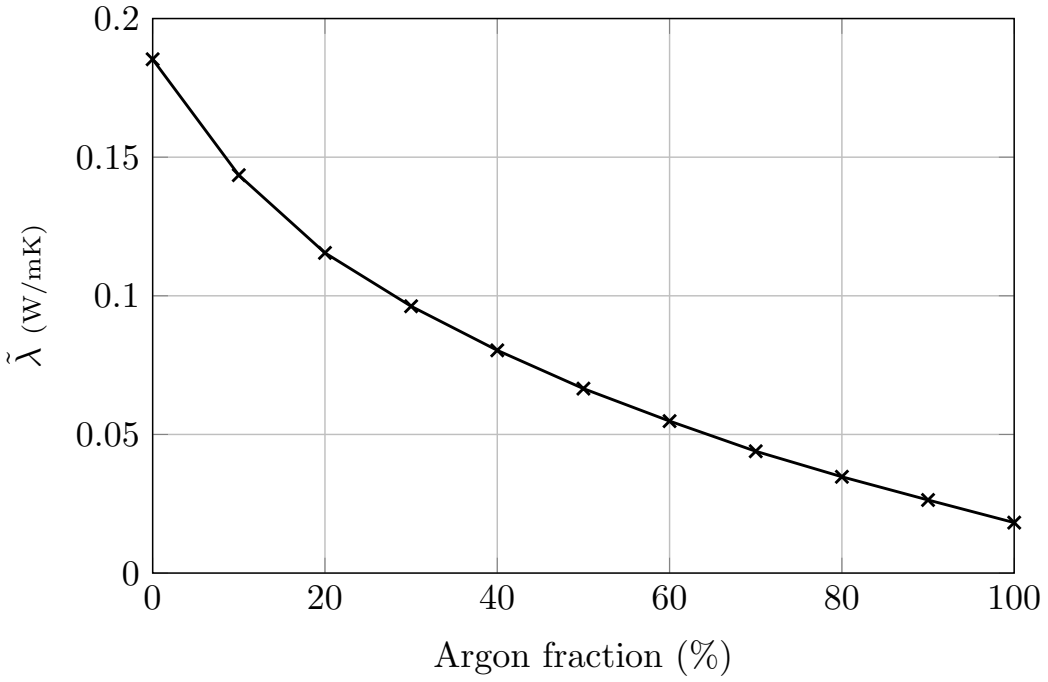

Figure B.16: Evolution of the thermal conductivity of an argon/dihydrogen gas mixture at 38 °C as a function of the argon fraction (Srivastava and Srivastava, 2004).

References

A. Bourgeat and A. Piatnitski. Approximations of effective coefficients in stochastic homogenization. In Annales de l'IHP Probabilités et statistiques, volume 40, pages 153–165, 2004.

R. Brandt and G. Neuer. Thermal conductivity and thermal radiation properties of UO_2. Journal of non-equilibrium thermodynamics, 1(1):3–24, 1976. doi: doi:10.1515/jnet.1976.1.1.3. URL https://doi.org/10.1515/jnet.1976.1.1.3.

S. Brisard and L. Dormieux. FFT-based methods for the mechanics of composites: A general variational framework. Computational Materials Science, 49(3):663–671, 2010.

S. Brisard, M. Schneider, and F. Willot. Introduction to FFT-based numerical methods for the homogenization of random materials. hal-03631887, 2022.

T. Calvet, J.M. Vanson, and R. Masson. A DEM/FFT approach to simulate the effective thermal conductivity of granular media. International Journal of Thermal Sciences, 172: 107339, 2022. ISSN 1290-0729. doi: https://doi.org/10.1016/j.ijthermalsci.2021.107339. URL https://www.sciencedirect.com/science/article/pii/S129007292100497X.

J. Carbajo, G. Yoder, S. Popov, and V. Ivanov. A review of the thermophysical properties of MOX and UO_2 fuels. Journal of Nuclear Materials, 299:181–198, 12 2001. doi: 10.1016/S0022-3115(01)00692-4.

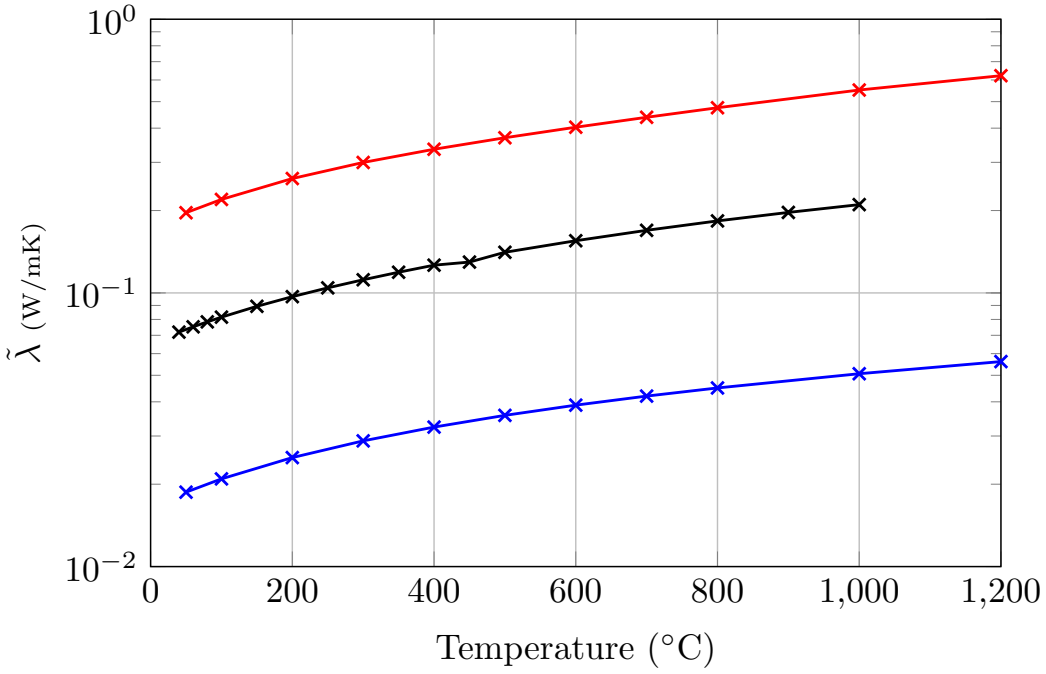

Figure B.17: The evolution of the conductivity of a 50-50 % argon/dihydrogen mixture as a function of temperature (Papari et al., 2005) – black curve – is compared to the one of pure argon – blue curve – and pure dihydrogen – red curve.

H. Cauwenbergh and W. Van Dael. Measurements of the thermal conductivity of gases: Iii. data for binary mixtures of helium and argon with hydrogen isotopes. Physica, 54(3): 347–360, 1971. ISSN 0031-8914. doi: https://doi.org/10.1016/0031-8914(71)90182-0. URL https://www.sciencedirect.com/science/article/pii/0031891471901820.

T. Chen, D. Chen, B.H. Sencer, and L. Shao. Molecular dynamics simulations of grain boundary thermal resistance in UO_2. Journal of Nuclear Materials, 452(1):364–369, 2014. ISSN 0022-3115. doi: https://doi.org/10.1016/j.jnucmat.2014.05.035. URL https://www.sciencedirect.com/science/article/pii/S002231151400302X.

N. Clozeau, M. Josien, F. Otto, and Q. Xu. Bias in the representative volume element method: periodize the ensemble instead of its realizations. Foundations of Computational Mathematics, pages 1–83, 2023.

T. Doualle, V. Le Guillous, V. Klosek, C. Onofri-Marroncle, M Reymond, L. Gallais, and Y. Pontillon. Development of UO_2 thermal diffusivity measurement with laser techniques. EPJ Web Conf., 253:07005, 2021. doi: 10.1051/epjconf/202125307005. URL https://doi.org/10.1051/epjconf/202125307005.

R. Drut. Caractéristiques thermodynamiques de l'Helium. Formules et Tables. 1968.

C Duguay and G Pelloquin. Fabrication of mixed uranium–plutonium carbide fuel pellets with a low oxygen content and an open-pore microstructure. Journal of the European Ceramic Society, 35(14):3977–3984, 2015.

E.R.G. Eckert, T.F. Irvine, and W.E. Ibele. Prandtl number, thermal conductivity, and viscosity of air-helium mixtures. Washington : National Aeronautics and Space Administration, 1960.

E.H.B. Fall. Extension de la méthode flash à de hautes températures. Mémoire de maîtrise, 1995.

J.K. Fink. Thermophysical properties of uranium dioxide. Journal of Nuclear Materials, 279(1):1–18, 2000. ISSN 0022-3115. doi: https://doi.org/10.1016/S0022-3115(99)00273-1. URL https://www.sciencedirect.com/science/article/pii/S0022311599002731.

J. Fourier. Théorie analytique de la chaleur. Paris : Chez Firmin Didot, père et fils, 1822.

L. Gélébart and R. Mondon-Cancel. Non-linear extension of FFT-based methods accelerated by conjugate gradients to evaluate the mechanical behavior of composite materials. Computational Materials Science, 77:430–439, 2013.

J.H. Harding and D.G. Martin. A recommendation for the thermal conductivity of UO_2. Journal of Nuclear Materials, 166(3):223–226, 1989. ISSN 0022-3115. doi: https://doi.org/10.1016/0022-3115(89)90218-3. URL https://www.sciencedirect.com/science/article/pii/0022311589902183.

Z. Hashin and S. Shtrikman. A variational approach to the theory of the elastic behaviour of multiphase materials. Journal of the Mechanics and Physics of Solids, 11(2):127–140, 1963. ISSN 0022-5096. doi: https://doi.org/10.1016/0022-5096(63)90060-7. URL https://www.sciencedirect.com/science/article/pii/0022509663900607.

B. Hay, J.R. Filtz, and J.C. Batsale. Mesure de la diffusivité thermique par la méthode flash. Techniques de l'ingénieur - CND : méthodes surfaciques base documentaire, 2017.

S. Hazanov and M. Amieur. On overall properties of elastic heterogeneous bodies smaller than the representative volume. International Journal of Engineering Science, 33(9):1289–1301, 1995.

R. Hill. Elastic properties of reinforced solids: Some theoretical principles. Journal of the Mechanics and Physics of Solids, 11(5):357–372, 1963. ISSN 0022-5096. doi: https://doi.org/10.1016/0022-5096(63)90036-X. URL https://www.sciencedirect.com/science/article/pii/002250966390036X.

IAEA. Thermophysical Properties Database of Materials for Light Water Reactors and Heavy Water Reactors. Number 1496 in TECDOC Series. INTERNATIONAL ATOMIC ENERGY AGENCY, Vienna, 2006. ISBN 92-0-104706-1. URL https://www.iaea.org/publications/7489/thermophysical-properties-database-of-materials-for-light-water-reactors-and-heavy-wa

S. Imura and E Takegoshi. Effect of gaz pressure on the effective thermal conductivity of packed beds. Heat Transfer Japanese Research, 3:13 – 26, 1974. doi: https://doi.org/10.1299/kikai1938.40.489.

Marc Josien. Merope: a microstructure generator for simulation of heterogeneous materials. Journal of Computational Science, page 102359, 2024. URL https://doi.org/10.1016/j.jocs.2024.102359.

T. Kanit, S. Forest, I. Galliet, V. Mounoury, and D. Jeulin. Determination of the size of the representative volume element for random composites: statistical and numerical approach. International Journal of Solids and Structures, 40(13):3647–3679, 2003. ISSN 0020-7683. doi: https://doi.org/10.1016/S0020-7683(03)00143-4. URL https://www.sciencedirect.com/science/article/pii/S0020768303001434.

D. J. Kim, Y. W. Rhee, J. H. Kim, K. S. Kim, J. S. Oh, J. H. Yang, Y. H. Koo, and K. W. Song. Fabrication of micro-cell UO_2-Mo pellet with enhanced thermal conductivity. Journal of Nuclear Materials, 462:289–295, 2015.

W.K. Kim, J.H Shim, and M. Kaviany. UO_2 bicrystal phonon grain-boundary resistance by molecular dynamics and predictive models. International Journal of Heat and Mass Transfer, 100:243–249, 2016. ISSN 0017-9310. doi: https://doi.org/10.1016/j.ijheatmasstransfer.2016.04.071. URL https://www.sciencedirect.com/science/article/pii/S0017931015313338.

B. Le Neindre. Conductivité thermique des liquides et des gaz. Techniques de l'ingénieur Caractérisation et propriétés de la matière, base documentaire : TIP510WEB. (ref. article : k427), 1998. doi: 10.51257/a-v1-k427. URL https://www.techniques-ingenieur.fr/base-documentaire/sciences-fondamentales-th8/equations-d-etats-et-constantes-thermiques-42340210/conductivite-thermique-des-liquides-et-des-gaz-k427/.

J.H Lienhard IV and J.H Lienhard V. A heat transfer textbook. 4th edition, Phlogiston Press, Cambridge, Massachusetts, 2017.

E. Litovsky, M. Shapiro, and A. Shavit. Gas pressure and temperature dependences of thermal conductivity of porous ceramic materials: Part 1, refractories and ceramics with porosity below 30%. Journal of the American Ceramic Society, 75:3425 – 3439, 03 2005. doi: 10.1111/j.1151-2916.1992.tb04445.x.

P.G. Lucuta, Hj. Matzke, and I.J. Hastings. A pragmatic approach to modelling thermal conductivity of irradiated UO_2 fuel: Review and recommendations. Journal of Nuclear Materials, 232(2):166–180, 1996. ISSN 0022-3115. doi: https://doi.org/10.1016/S0022-3115(96)00404-7. URL https://www.sciencedirect.com/science/article/pii/S0022311596004047.

J. B. MacEwan, R. L. Stoute, and M. J. F. Notley. Effect of porosity on the thermal conductivity of UO_2. Journal of Nuclear Materials, 24(1):109–112, 1967.

D. Maillet, C. Moyne, and B. Rémy. Effect of a thin layer on the measurement of the thermal diffusivity of a material by a flash method. International Journal of Heat and Mass Transfer, 43(21):4057–4060, 2000. ISSN 0017-9310. doi: https://doi.org/10.1016/S0017-9310(00)00020-X.

D.G. Martin. The thermal expansion of solid UO_2 and (U, Pu) mixed oxides - a review and recommendations. Journal of Nuclear Materials, 152(2):94–101, 1988. ISSN 0022-3115. doi: https://doi.org/10.1016/0022-3115(88)90315-7. URL https://www.sciencedirect.com/science/article/pii/0022311588903157.

J.C. Maxwell. A Treatise on Electricity and Magnetism, volume 1 of Cambridge Library Collection - Physical Sciences. Cambridge University Press, 1873. doi: 10.1017/CBO9780511709333.

J. Meynard, M. Ibrahim, A. Monnier, M. Bornert, E. Castelier, C. Duguay, M. Garajeu, and R. Masson. Effective properties of an isotropic solid weakened by micro-cracks located at inter-granular boundaries. Journal of the Mechanics and Physics of Solids, 158:104647, January 2022. doi: 10.1016/j.jmps.2021.104647. URL https://hal.archives-ouvertes.fr/hal-03379552.

M. Moscardini, Y. Gan, S. Pupeschi, and M. J. F. E. Kamlah. Discrete element method for effective thermal conductivity of packed pebbles accounting for the Smoluchowski effect. Fusion Engineering and Design, 127:192–201, 2018.

H. Moulinec and P. Suquet. A fast numerical method for computing the linear and nonlinear mechanical properties of composites. Comptes rendus de l'Académie des sciences. Série II, Mécanique, physique, chimie, astronomie, 318(11):1417–1423, 1994. ISSN 1251-8069.

L. Moutin. Caractérisation et modélisation du réseau poreux de microstructures céramiques UO_2 : Application à la simulation de la conductivité thermique de ces microstructures à différentes températures et dans différents environnements. PhD thesis, 2023.

L. Moutin, J. Meynard, M. Josien, M. Bornert, C. Duguay, F. Adenot, V. Bouineau, L. Fayette, and R. Masson. Realistic morphological models of weakly to strongly branched pore networks for the computation of effective properties. International Journal of Solids and Structures, page 112249, 2023. ISSN 0020-7683. doi: https://doi.org/10.1016/j.ijsolstr.2023.112249. URL https://www.sciencedirect.com/science/article/pii/S0020768323001464.

L. Moutin, J. Meynard, M. Bornert, C. Duguay, F. Adenot, V. Bouineau, L. Fayette, and R. Masson. Morphological models of networks of inter-granules micro-cracks: identification and validation based on 2D and 3D imaging. Proceedings in Mathematics and Statistics, 2024.

Gerhard Ondracek and Brigitte Schulz. The porosity dependence of the thermal conductivity for nuclear fuels. Journal of Nuclear Materials, 46(3):253–258, 1973.

M.M. Papari, D. Mohammad-aghaiee, B. Haghighi, and A. Boushehri. Transport properties of argon–hydrogen gaseous mixture from an effective unlike interaction. Fluid Phase Equilibria, 232(1):122–135, 2005. ISSN 0378-3812. doi: https://doi.org/10.1016/j.fluid.2005.03.022. URL https://www.sciencedirect.com/science/article/pii/S0378381205000865.

W.J. Parker, R.J. Jenkins, and C.P. Butler. Flash method of determining thermal diffusivity, heat capacity and thermal conductivity. Journal of Applied Physics, Volume 32.9, p1679-1684, 1961. doi: https://doi.org/10.1063/1.1728417.

S. Phillpot, A. El-Azab, A. Chernatynskiy, and J. Tulenko. Thermal conductivity of UO_2 fuel: Predicting fuel performance from simulation. JOM, 63:73–79, 08 2011. doi: 10.1007/s11837-011-0143-x.

P. Pinot. Détermination de la porosité de roches calcaires : méthode et incertitude de mesure. Revue française de métrologie, 37 2015-1:37–53, 2015. doi: https://doi.org/10.1051/rfm/2015004.

M. Schneider. A review of nonlinear FFT-based computational homogenization methods. Acta Mechanica, 232(6):2051–2100, 2021.

M. Schneider, M. Josien, and F. Otto. Representative volume elements for matrix-inclusion composites - a computational study on the effects of an improper treatment of particles intersecting the boundary and the benefits of periodizing the ensemble. Journal of the Mechanics and Physics of Solids, 158:104652, 2022. ISSN 0022-5096. doi: https://doi.org/10.1016/j.jmps.2021.104652. URL https://www.sciencedirect.com/science/article/pii/S0022509621002891.

B. N. Srivastava and R. C. Srivastava. Thermal Conductivity and Eucken Correction for Diatomic Gases and Binary Gas Mixtures. The Journal of Chemical Physics, 30(5):1200–1205, 08 2004. ISSN 0021-9606. doi: 10.1063/1.1730155. URL https://doi.org/10.1063/1.1730155.

K. Stephan and A. Laesecke. The Thermal Conductivity of Fluid Air. Journal of Physical and Chemical Reference Data, 14(1):227–234, 01 1985. ISSN 0047-2689. doi: 10.1063/1.555749. URL https://doi.org/10.1063/1.555749.

S. Torquato and H.W. Haslach Jr. Random heterogeneous materials: Microstructure and macroscopic properties. Applied Mechanics Reviews, 55(4):B62–B63, 07 2002. ISSN 0003-6900. doi: 10.1115/1.1483342. URL https://doi.org/10.1115/1.1483342.

L. Vlahovic, D. Staicu, A. Küst, and R.J.M. Konings. Thermal diffusivity of UO_2 up to the melting point. Journal of Nuclear Materials, 499:504–511, 2018. ISSN 0022-3115. doi: https://doi.org/10.1016/j.jnucmat.2017.11.050. URL https://www.sciencedirect.com/science/article/pii/S0022311517301976.

X. Yang, J. Tiwari, and T. Feng. Reduced anharmonic phonon scattering cross-section slows the decrease of thermal conductivity with temperature. Materials Today Physics, 24: 100689, 2022.